

1 **Multi-year black carbon observations and modeling close to the**
2 **largest gas flaring and wildfire regions (Western Siberian Arctic)**

3 **Olga B. Popovicheva¹, Marina A. Chichaeva², Nikolaos Evangeliou^{3,*}, Sabine Eckhardt³,**
4 **Evangelia Diapouli⁴, and Nikolay S. Kasimov²**

5
6 ¹SINP, Lomonosov Moscow State University, 119991 Moscow, Russia

7 ²Faculty of Geography, Lomonosov Moscow State University, 119991 Moscow, Russia

8 ³NILU, Department for Atmospheric & Climate Research (ATMOS), 2007 Kjeller, Norway

9 ⁴ERL, Institute of Nuclear and Radiological Science & Technology, Energy & Safety, NCSR
10 Demokritos, 15341 Attiki, Athens, Greece

11 * Corresponding author: N. Evangeliou (Nikolaos.Evangeliou@nilu.no)

12

13

14 **Abstract**

15 The influence of aerosols on the Arctic system remains associated with significant
16 uncertainties, particularly concerning black carbon (BC). The polar aerosol station "Island Bely"
17 (IBS), located in Western Siberian Arctic, was established to enhance aerosol monitoring.
18 Continuous measurements from 2019 to 2022 revealed the long-term effects of light-absorbing
19 carbon. During the cold period, the annual average light absorption coefficient was $0.7 \pm 0.7 \text{ Mm}^{-1}$,
20 decreasing by 2-3 times during the warm period. The interannual mean showed a peak in February
21 ($0.9 \pm 0.8 \text{ Mm}^{-1}$), a ten times lower minimum in June, and exhibited high variability in August (0.7
22 $\pm 2.2 \text{ Mm}^{-1}$). An increase of up to 1.5 at shorter wavelengths from April to September suggests
23 contribution from brown carbon (BrC). The annual mean equivalent black carbon (*eBC*)
24 demonstrated considerable interannual variability, with the lowest in 2020 ($24 \pm 29 \text{ ng m}^{-3}$).
25 Significant difference was observed between Arctic Haze and Siberian wildfire periods, with
26 record-high pollution levels in February 2022 ($110 \pm 70 \text{ ng m}^{-3}$) and August 2021 ($83 \pm 249 \text{ ng}$
27 m^{-3}). Anthropogenic BC contributed 83% to the total for the entire study period and gas flaring,
28 domestic combustion, transportation, and industrial emissions dominated. During the cold season,
29 >90% of surface BC was attributed to anthropogenic sources, mainly gas flaring. In contrast, during
30 the warm period, Siberian wildfires contributed to BC concentrations by 48%. In August 2021,
31 intense smoke from Yakutian wildfires was transported at high altitudes during the region's worst
32 fire season in 40 years.

33

34

1 Introduction

Multiple socio-economic drivers and feedbacks, including air pollution (Arnold et al., 2016) influence the natural and human environment of the Arctic. Over the last few decades, the Arctic warms more than three times faster than the global average (AMAP, 2021). The pronounced rapid changes affect atmospheric transport and aerosol relative source contributions (Heslin-Rees et al., 2020). Drier conditions and warmer temperatures are the main cause of enhanced fire activity. Boreal forest fires become more frequent and severe (Rogers et al., 2020), especially in Central Siberia, and Northern America (Kasischke and Turetsky, 2006; Kharuk and Ponomarev, 2017; Veraverbeke et al., 2017). Widespread smoke plumes, particularly in Siberia, lead to substantial deterioration of air quality increasing fine particulate matter (Silver et al., 2024).

Interactions between aerosol and different cloud types, available solar radiation, sea ice, surface albedo, Arctic and lower latitude removal processes, and atmospheric transport patterns. affect Arctic pollution and its climate impacts (Willis et al., 2018), such as the Arctic haze (namely the persistent Arctic air pollution during late winter and early spring). To understand such phenomena and thus reduce their impact, there is a clear need for comprehensive studies of the climate-relevant aerosol processes that occur in the Arctic. A species of major concern is BC, a short-lived climate forcer (Schmale et al., 2021). BC is emitted from the incomplete combustion of fossil fuel and biomass; it is defined as the portion of carbonaceous aerosols, which absorb strongly in the entire climate relevant wavelength region of the solar spectrum (i.e. IR-VIS-UV). BC contributes to Arctic warming in multiple ways (e.g., Lee et al., 2013), including the darkening effect of BC deposited on snow and ice (Flanner, 2013). AMAP (2015) reports that the Arctic equilibrium temperature response is (+0.4°C) due to forcing from atmospheric BC and (+0.22°C) due to snow BC.

At present, the largest uncertainties when assessing aerosol impact on the climate are attributed to BC (AMAP, 2021). To follow-up on this, BC measurements are taken at various polar regions in the European, Siberian, and Canadian Arctic (Stone et al., 2014; Yttri et al., 2014; Popovicheva et al., 2019a; Winiger et al., 2019; Manousakas et al., 2020; Gilardoni et al., 2023). For instance, Stathopoulos et al. (2021) reported on the long-term impact of light-absorbing carbon in the high Arctic by analysing 15 years of data from the Zeppelin station (Svalbard), while Schmale et al. (2022) studied the status of the Arctic haze peak concentrations at 10 Arctic observatories.

There is a large diversity in magnitude and variability of aerosol optical properties, reflecting differences in sources throughout the Arctic (Schmeisser et al., 2018). BC measurements are based on various instrumentations and methods that increase uncertainty (Sharma et al., 2017; Asmi et al.,

2021; Ohata et al., 2021). The optical properties of BC have been previously evaluated against direct mass measurements techniques (Sharma et al., 2004; Eleftheriadis et al., 2009; Yttri et al., 2024). The conversion of light attenuation to absorbing carbon mass concentration is performed by the mass-specific absorption coefficient (*MAC*) (Petzold et al., 2013) that is highly influenced by the aerosol mixing state and non-BC light-absorbing species such as organic matter and mineral dust (Zanatta et al., 2018) and varies in time and space depending on sources and transformations during transport (Bond et al., 2013; Chen et al., 2023). Therefore, it is crucial to quantify the contribution of non-BC component and aging in order to determine the actual *MAC* value experimentally at each site (Singh et al., 2024).

The *AAE* defined as the relative fraction of wavelength - dependence of absorption of BC versus other light absorbing constituents, also differs from site to site (Schmeisser et al., 2018). A fraction of organic aerosol, the BrC, increases the aerosol absorbing properties at short UV-VIS wavelengths (Sandradewi et al., 2008; Grange et al., 2020; Helin et al., 2021) and dominates the absorption during wildfire seasons (Bali et al., 2024). BrC originates mainly from biomass burning (BB) and can impose strong warming effect in the Arctic, especially in the summertime (Yue et al., 2022).

Despite its remoteness, the Arctic is one of the main receptors of anthropogenic air pollutant emissions from the Northern Hemisphere (Stohl et al., 2013). BC trends and seasonality at three Arctic sites, Alert (Canadian Arctic), Barrow/Utqiagvik (American Arctic), and Zeppelin, Ny-Ålesund (European Arctic) reveal a negative trend of 40% over 16 years due to the anthropogenic emission reduction (Sharma et al., 2013). The recent increase in fires and their earlier starts, due to the ongoing warming, have made wildfires in the Northern Eurasia a significant source of Arctic BC (Evangelizou et al., 2016). Fossil fuel combustion is the major source of BC in the Arctic troposphere (50–94%) (55–68% at the surface and 58–69% in the snow) and BB dominates at certain altitudes (600–800 hPa) between April to September (Qi and Wang, 2019). This agrees with Matsui et al. (2022) who reported that the largest contribution to Arctic BC is from BB sources in Siberia travelling at high altitudes.

Northern Eurasia, particularly Siberia, is a key source region of pollution in the Arctic. Source quantification (Zhu et al., 2020) shows that surface Arctic BC originates mainly from anthropogenic emissions in Russia (56%). The reason for this is that the largest oil and gas producing facilities of Western Siberia are located along the main pathway of air masses that enter the Arctic and thus have a disproportionately large contribution to the Arctic lower troposphere (Stohl, 2006; Stohl et al., 2013). Eleftheriadis et al. (2009) and Tunved et al. (2013) identified these regions as a key source for the highest measured BC in the European Arctic. The impact of long-range transport from these

regions has been previously reported in Ice Cape Baranova station (Manousakas et al., 2020) and Tiksi (Northeastern Siberia) (Winiger et al., 2017; Popovicheva et al., 2019a). Airborne observations over the coast of the Arctic seas have identified the long-term transport of the industrial pollution (Zenkova et al., 2022). Furthermore, efforts have sought to develop BC emission inventories for the Siberian Arctic, based on activity data from local information, improved gas flaring emissions, and satellite data (Huang et al., 2015; Böttcher et al., 2021; Kostykin et al., 2021; Vinogradova and Ivanova, 2023). To better quantify the source contribution to the Arctic environment, targeted aerosol measurements close to the flaring facilities are needed. The present operating Eurasian Arctic stations are all too far away to allow assessing how air masses are affected by different source categories (Stohl et al., 2013). However, ship campaigns focusing on BC close to main source regions (e.g., gas flaring facilities of the Western Siberia) have provided a better constraint of how anthropogenic and BB sources influence Arctic pollution (Popovicheva et al., 2017b).

Another major source of the Arctic BC is wildfires in the Siberian and Far Eastern regions, which have grown in recent summers (Bondur et al., 2020). Airborne observations of BC in Siberia have confirmed impact forest fires (Paris et al., 2009). Eastern Siberia (Yakutia) has been prone to large wildfires due to a combination of hot summers ($> 40^{\circ}\text{C}$) and low humidity (Tomshin and Solovyev, 2022). For instance, wildfires in summer 2019 in Eastern Siberia occurred along the trans-Arctic transport pathway resulting in enhanced aerosol load observed in Western Canada (Johnson et al., 2021). BB emissions occurring at midlatitudes reached the European Arctic in 2020 influencing aerosol composition (Gramlich et al., 2024).

Despite the necessity for detailed observations in the Northwestern Siberia, a dense observational network is still absent. Towards this, the polar aerosol station on the Bely Island (Kara Sea, Western Siberia) started to operate in August 2019 (Popovicheva et al., 2022, 2023). The significance of high-quality measurements at the IBS is documented, as the station is located along the main pathway of large-scale emission plumes from industrial regions and Siberian wildfires entering the Arctic (Popovicheva et al., 2022). Further investigation performed at IBS in August 2021 showed impact from a long-range transport event with unprecedented high concentrations of carbonaceous aerosol (Schneider et al., 2024).

In this paper, we show improved light absorption long-term measurements and BC seasonal and inter-annual variability in the Western Siberian Arctic from three and a half years (2019-2022) of observations at IBS. BC was calculated in two ways: as *eBC* by an aethalometer and as elemental carbon (EC) by thermal-optical analysis. We further evaluate the seasonal changes in the observed absorption coefficients. Seasonal difference in intensive optical properties is shown by the

wavelength-dependent *AAE*, which acts as indication of the BrC impact. Estimated site-specific absorption coefficient (*SAC*) considered the specific seasonal effects of mixing and aging of aerosols at IBS. We further assess the inter-annual variability of origin, transport and main BC sources using modelling tools coupled with the most recent anthropogenic and BB emission datasets.

2 Methods

2.1 Polar aerosol Island Bely station, location and meteorology

The aerosol IBS of Moscow State University (73020'7.57"N, 70040'49.05"E) is shown in **Figure 1a** together with other Polar Arctic observatories. Western Siberia is the world's largest gas flaring region with a leading oil and gas production industry (**Figure 1b**). It is also an area under intensive exposure by Siberian wildfires (Tomshin and Solovyev, 2022; Voronova et al., 2022). A satellite image of smoke plume for 5th August 2021 was obtained from <https://worldview.earthdata.nasa.gov>. Fires are shown from the Fire Information for Resource Management System (FIRMS) (<https://firms.modaps.eosdis.nasa.gov/map>) ten days back in time.

The climate at IBS is characterized by a large annual variability determined by alternating periods of the polar night and midnight sun. Basic meteorological parameters, such as temperature, wind speed and direction were obtained every 3 hours from a meteorological station located 500 m away from the IBS. The cycles of temperature, precipitation, snow coverage, wind speed and relative humidity are shown in **Figure S 1**. Annual temperature varied from -39°C to 23°C (mean: -6±12°C) (**Table S 1**). For further analysis, we have split the annual cycle in two periods based on the prevailing temperatures, November-April ("cold period", -15.9±9.1) and May - October ("warm period", 2.8±5.8). High relative humidity of 87±8% was typical for the study period, with less than 80% observed in winter 2020. Precipitation was maximum in summer (22 mm) with constant snow coverage from October to May. Wind was relatively stable, with a mean speed of 6±3 m s⁻¹, which increased in winter up to 17 m s⁻¹ (**Figure S 1**).

Wind patterns for the cold period in **Figure S 1** show a prevailing wind direction from south, southwest, and southeast. Winds were predominantly continental, rarely occurring from the ocean; significant emission sources from the continent were downwind. In the warm period, the wind patterns were more spatially homogeneous with northeastern direction. Period from June and September was characterized by a frequent occurrence of oceanic air masses and constant wind speeds.

2.2 Aerosol optical and chemical characterization

The aerosol pavilion is situated approximately half a km to the southeast of the meteorological station. An aerosol sampling system composed from three total suspended particle inlets has been installed approximately 1.5 m above the roof and 4 m above the ground. They are equipped with an electric heating wire to prevent rimming and ice blocking of the system. One inlet was used for the real-time light-absorption measurements with air flow 5 L min⁻¹. Two other inlets low-volume samplers (Derenda, Germany) were used for sampling of total suspended particles (TSP) operating at 2.3 m³ h⁻¹ flow (0°C, 1013.25 hPa).

An Aethalometer model AE33 (Magee Scientific, Aerosol d.o.o.) was used to measure the light attenuation caused by particles deposited on two filter spots at different flow rates (Drinovec et al., 2015) and at seven wavelengths from ultraviolet (370 nm) to infrared (950 nm). The “dual spot” technique is applied for real-time loading effect compensation. Optical absorption of aerosols on the filter is influenced by scattering of light within the filter; the enhancement of optical absorption is described by the factor *C* that depends on the filter material. The producer recommends an enhancement factor of 1.57 for TFE-coated glass fiber filter. The light-absorbing content of carbonaceous aerosol is reported as *eBC* concentration by aethalometer (*eBC_{AET}*) for the given wavelength λ , which is determined for each time interval from the change in the light absorption using the *MAC*. The aerosol optical absorption coefficient (*b_{abs}*) is therefore:

$$b_{abs}(\lambda) = eBC_{AET}(\lambda) \times MAC(\lambda) \quad (1)$$

where *eBC_{AET}* at 880 nm is determined using the *MAC* of 7.7 m² g⁻¹. The aerosol optical absorption coefficient for different wavelengths is determined with their *MAC* values that are equal to 11.58, and 13.14 m² g⁻¹ at 590, and 520 nm, respectively.

To represent the spectral dependence of the light absorption, the *AAE* was derived by using a fitted power law relationship:

$$b_{abs}(\lambda) = b_{abs}(\lambda_o) \times \left(\frac{\lambda}{\lambda_o}\right)^{-AAE} \quad (2)$$

where *b_{abs}*(λ_o) is the absorption coefficient at the reference wavelength λ_o , *AAE* is a measure of strength of the spectral variation of aerosol light absorption.

BC absorbs strongly in the NIR-VIS (near-infrared and visible) with only moderate increment towards the shorter wavelengths. Light absorbing organic components related to BrC absorb light at shorter wavelengths more effectively than at 880 nm, which is observed as an increased *AAE* (Sandradewi et al., 2008; Grange et al., 2020; Helin et al., 2021). The total light absorption is assumed to include the contribution of both BC and BrC (Ivančič et al., 2022):

$$b_{abs}(\lambda) = b_{abs/BC}(\lambda) + b_{abs/BrC}(\lambda) \quad (3)$$

Using Eq. 1, the BrC absorption becomes: $b_{abs/BrC}(\lambda) = b_{abs}(\lambda) - b_{abs}(\lambda_0) \times \left(\frac{\lambda}{\lambda_0}\right)^{-AAE}$ (4)

Light-absorption measurements were performed for three and a half years, from 10 August 2019 to 31 December 2022, with a time resolution of 1 min. Data were cleaned based on analysis of meteorological parameters by examining whether the wind originated from the direction of the meteorological station where diesel generators operated. In such cases, strong peaks of BC were removed from further analysis. Around 6.4 % of the hourly-average data were cleaned from the dataset due to local pollution impact. To avoid the instrumental noise when calculating the AAE, the z-score was used that calculates the ratio of difference between a single raw data value and the data mean to the data standard deviation. Outliers (< -3 and > 3 of observation's z-score) were removed from the dataset.

A thermal EC analysis was conducted for the samples in parallel to AE33. Sampling was performed on 47 mm quartz fiber (Pallflex) filters preheated at 600°C for 5 h. The low concentrations of ambient aerosols necessitate that the sampling times reach up to a week, in order to allow the filter loading to exceed the detection limit for relevant aerosol chemistry analyses. The total number of samples limited by the low detection limit of the thermal-optical instrument were 180.

Organic (OC) and EC were measured by thermo-optical transmittance (TOT) analysis (Lab OC-EC Aerosol Analyzer, Sunset Laboratory, Inc.) using the methodology reported in Popovicheva et al. (2019) and Manousakas et al. (2020). Quartz filter samples were heated first up to 650 °C in He atmosphere and then up to 850 °C in a mixture of 2% O₂ in He, using the controlled heating ramps of the EUSAAR_2 thermal protocol. OC evolves in inert atmosphere, while the thermal refractory fraction EC is oxidized in the He-O₂ atmosphere. Charring correction due to pyrolytic carbon was applied by monitoring the sample transmittance throughout the heating process. The limit of detection for the EC analysis was 0.05 µg C cm⁻². QA/QC procedures of EN 16909:2017 were also applied during TOT analysis. Laboratory and field blanks were prepared and ran following the same analytical procedures as for the samples.

Both methods have important uncertainties (10 - 80%, Sharma et al., 2017; Ohata et al., 2021). The determination of EC by thermo-optical analysis may be impacted by the presence of carbonate carbon (CC), which is quantified during analysis as OC and/or EC. The contribution of CC in fine aerosol is generally considered negligible but its interference may be significant for coarse aerosol and samples heavily impacted by resuspended soil. The split between EC and OC

may be also affected by the presence of light-absorbing species others than EC, such as light absorbing organic carbon. In addition, the presence of mineral oxides, such as iron oxide, might provide oxygen during analysis and lead to pre-oxidation of EC in inert atmosphere. *eBC* might overestimate BC if there are coexisting components such as BrC (Chakrabarty et al., 2010) and dust (Petzold et al., 2009). In addition, the aethalometer response depends on filter loading and multiple scattering by the filter medium and sampled aerosol particles (Backman et al., 2017).

Validations of *eBC* retrievals were performed against results from thermal-optical analysis of EC according to an approach that has been used previously in Sharma et al. (2004), Eleftheriadis et al. (2009) and Yttri et al. (2014). To convert optical absorption at 880 nm to BC mass, the *SAC* was estimated as:

$$SAC = \frac{b_{abs/BC}}{EC} \quad (5)$$

Data processing was performed using Deming's total least-squares regression to compare measurements from different methods and modelling, estimate the *MAC*, and evaluate correlations among variables (R package "Deming"; (Therneau, 2024)). Deming regression fits a couple of variables considering the independent errors of both. The errors are assumed to be normally distributed; the error ratio is 1, and the regression results are equivalent to the orthogonal regression with the intercept forced through zero.

2.3 Atmospheric dispersion modelling and emission inventories

To investigate the air mass transport and possible origin of BC during the study period (2019 – 2023), the Lagrangian particle dispersion model FLEXPART version 10.4 was used (Pisso et al., 2019) driven by hourly reanalysis meteorological fields (ERA5) from the European Centre for Medium-Range Weather Forecasts (ECMWF) with 137 vertical levels (up to approximately 80 km) and a horizontal resolution of $0.5^\circ \times 0.5^\circ$ (Hersbach et al., 2020). In FLEXPART, computational particles were released at heights 0 - 100 m from the receptor (IBS) and tracked backward in time in FLEXPART's "retroplume" mode. Simulations extended over 30 days backward in time, sufficient to include most BC emissions arriving at the station, given a typical BC lifetime of 1 week (Bond et al., 2013). The tracking includes gravitational settling for spherical particles, dry and wet deposition of aerosols (Grythe et al., 2017), turbulence (Cassiani et al., 2015), unresolved mesoscale motions (Stohl et al., 2005), and deep convection (Forster et al., 2007). The FLEXPART output consists of a footprint emission sensitivity that expresses the probability of any emission occurring in each grid-cell to reach the receptor. The footprint can be converted to modelled concentration at the receptor, when coupled with gridded emissions from an emission inventory. Modelled concentrations can be calculated as a function of the time elapsed since the emission has occurred (i.e., "age"), which can

265 be shown as “age spectrum”, while masks of specific regions/continents can give the continental
266 contribution to the simulated concentration (i.e., “continent spectrum”).

267 The source contribution to receptor BC is calculated by combining each gridded emission
268 sector (e.g. gas flaring, transportation, waste management etc...) from an emission inventory with
269 the footprint emission sensitivity (as described in the previous paragraph). Calculations for
270 anthropogenic sources (emission sectors are described below) and open BB were performed
271 separately. This enabled identification of the exact origin of BC and allowed for quantification of its
272 source contribution. Anthropogenic emissions were adopted from the latest version (v6b) of the
273 ECLIPSE (Evaluating the CLimate and Air Quality ImPacts of ShortlivEd Pollutants) dataset, an
274 upgraded version of the previous version (Klimont et al., 2017). The inventory includes emissions
275 from industrial combustion (IND), from the energy production sector (ENE), residential and
276 commercial emissions (DOM), emissions from waste treatment and disposal sector (WST),
277 transportation (TRA), shipping activities (SHP) and gas flaring emissions (FLR). The methodology
278 for obtaining emissions from FLR specifically over the Russian territories has been improved in
279 ECLIPSEv6 (Böttcher et al., 2021). Annual total and monthly anthropogenic emissions are shown
280 in **Figure S 2**. BB was adopted from the Copernicus Global Fire Assimilated System (CAMS
281 GFAS) (Kaiser et al., 2012) because this product provides an estimation of the injection altitude of
282 the fire emissions that is crucial for accurate simulation of the BB dispersion. Annual total and daily
283 fire emissions from CAMS GFAS are shown in **Figure S 3**.

284 **3 Results**

285 **3.1 Aerosol light-absorption**

286 Light-absorption coefficients at 880 nm, $b_{abs}(880)$ were used to infer eBC mass
287 concentrations. $b_{abs}(880)$ were plotted as hourly and monthly means during the entire study period
288 (2019-2022) (**Figure 2**). **Table 1** presents the data statistical summary. The mean \pm sigma (median)
289 value of $b_{abs}(880)$ was 0.5 ± 0.9 (0.27) Mm^{-1} for the entire study period. In the cold period the
290 annual average mean (median) of $b_{abs}(880)$ was 0.7 ± 0.7 Mm^{-1} (0.5), during the warm period it
291 was 1.9 (2.5) times less. There is a clear seasonality consistent with the Arctic aerosol light
292 absorption from other studies (Stathopoulos et al., 2021; Schmale et al., 2022; Pulimeno et al.,
293 2024) due to the formation of the polar dome and the slow removal processes in the Arctic in winter
294 (Law and Stohl, 2007). 15 years (2001-2015) record at Zeppelin demonstrated that the long-term
295 seasonality of light absorbing carbon (Stathopoulos et al., 2021) $b_{abs}(880)$ was $0.112 Mm^{-1}$

296 (median) in the cold period and 0.035 Mm^{-1} in the warm period; both values approximately 5 times
297 less than those observed at IBS.

298 Monthly means of $b_{abs}(880)$ for each year together with intra-annual means for IBS are
299 shown in **Figure 2**. Specifically, annual average $b_{abs}(880)$ exhibits a significant peak during
300 winter and summer for any year. The examination of the overall changes by the inter-annual mean
301 reveals a gradual increase from November ($0.4 \pm 0.5 \text{ Mm}^{-1}$) to February ($0.9 \pm 0.8 \text{ Mm}^{-1}$); the latter
302 represents the maximum light absorption observed at IBS. In February, the monthly mean of
303 $b_{abs}(880)$ ranged from 0.4 to 1.7 Mm^{-1} reaching the maximum (1.7 Mm^{-1}) in 2022. Thus, Arctic
304 haze is present at IBS in winter months, from December to February. Starting from March (0.6 ± 0.5
305 Mm^{-1}), the inter-annual mean decreased down to a minimum in June ($0.1 \pm 0.2 \text{ Mm}^{-1}$) that was 9
306 times less than that of February. August had the highest light-absorption (mean: $0.7 \pm 2.2 \text{ Mm}^{-1}$)
307 within the summer months, ranging from 0.2 to 1.5 Mm^{-1} and showing a maximum of 1.5 in 2021.
308 September and October demonstrated a similar level of variability with June. At Zeppelin, the
309 maximum of the intra-annual (2001-2015) mean was seen in March - April (0.3 Mm^{-1})
310 (Stathopoulos et al., 2021), coinciding with the Arctic haze phenomenon in late winter-spring that
311 has been widely observed in the European and Canadian Arctic (Sharma et al., 2004; Schmale et al.,
312 2022).

313 In order to relate the light absorption in visible spectrum to the variability on other locations
314 (Schmeisser et al., 2018; Pulimeno et al., 2024), we calculate b_{abs} at 520 and 590 nm. The mean
315 (median) value of $b_{abs}(520)$ was 0.9 ± 1.6 (0.5) Mm^{-1} for the entire study period (**Table I**). At Ny-
316 Ålesund (Svalbard), the annual mean (median) $b_{abs}(530)$ averaged for 2018 to 2022 was 0.22
317 (0.13) Mm^{-1} (Pulimeno et al., 2024), approximately 4 times less. Moreover, the absorption
318 coefficient $b_{abs}(550)$ of 0.18 (0.09) Mm^{-1} recorded for 2012-2014 again in Svalbard (Schmeisser
319 et al., 2018) was 4 times less compared to annual average light absorption at IBS.

320 We present multi-annual box-and-whisker plots of b_{abs} at 590 nm in **Figure 3**. The
321 wavelength of 590 nm was chosen as the closest to 550 nm reported for the polar station Tiksi
322 (Schmeisser et al., 2018; Schmale et al., 2022). The monthly medians of $b_{abs}(590)$ in February
323 ranged from 0.3 to 2.3 Mm^{-1} , representing the highest values observed in 2022. The highest
324 extended interquartile range (up to 1 Mm^{-1}) was observed in the cold period. Conversely, the
325 summer months exhibited a minimum of approximately 0.1 Mm^{-1} for $b_{abs}(590)$ with smaller
326 variation of data characterized by the low interquartile range of 0.4 Mm^{-1} .

327 The annual cycle of $b_{abs}(590)$ reflects the higher aerosol burden during the haze season and
328 the low concentrations during summer at Alert, Barrow/Utqiagvik, Zeppelin, Gruvebadet, and Tiksi

(Schmale et al., 2022). Seasonality of b_{abs} medians at 550 nm for polar stations (Alert, Barrow/Utqiagvik, Tiksi, Zeppelin) from (Schmeisser et al., 2018) and $b_{abs}(590)$ for IBS are presented in **Figure 3**. All sites demonstrate similar seasonal variations, albeit a different magnitude of light absorption. In February, the maximum $b_{abs}(590)$ (1.1 Mm^{-1}) was observed at IBS; a higher value has been only observed at Tiksi which is explained by the influence from local sources (Popovicheva et al., 2019a). Other stations show the Arctic haze maximum later (in March or April); a sharp decline of $b_{abs}(590)$ was observed at those months at IBS. Values similar to other Arctic stations were recorded at IBS in June, with an annual minimum of around 0.1 Mm^{-1} . Since July, $b_{abs}(590)$ at IBS was higher than at other stations except Tiksi and peaked at 0.8 Mm^{-1} in December. The polar station Pallas exhibits the opposite behaviour peaking in spring and summer (Schmeisser et al., 2018). Pallas is located relatively south as compared to the rest of the polar stations and, hence, it is influenced by anthropogenic and biogenic emissions from surrounding boreal forests (Asmi et al., 2011). Aerosol optical properties in the IR and visible solar spectrum at IBS are different from European, Canadian and Western high-latitude polar locations due to different source origins, but light absorption coefficients are higher during the haze period (December-February).

3.2 Black carbon and site-specific mass absorption cross-section

EC collocated with light absorption observations is widely used to infer BC (Grange et al., 2020). **Figure 4a** shows concentrations of EC determined for samples collected in parallel with the aethalometer measurements from 10 August 2019 to 31 December 2022, with eBC_{AET} concentrations averaged over the sampling period. Both weekly EC and eBC_{AET} concentrations show the same seasonal variations with a maximum in winter and minimum in summer. EC concentrations are generally smaller than eBC_{AET} . The annual EC mean concentrations ranged from 6.5 to 16.3 ng C m^{-3} . The highest EC ($0.2 \text{ } \mu\text{g C m}^{-3}$) was recorded in December 2019 and the highest eBC_{AET} ($0.4 \text{ } \mu\text{g m}^{-3}$) in December 2019 and January 2022. EC was higher ($0.05 \pm 0.03 \text{ } \mu\text{g C m}^{-3}$) in the cold period and decreased ($0.02 \pm 0.03 \text{ } \mu\text{g C m}^{-3}$) in the warm period (**Table I**). Annual average mean EC during the entire study period was $0.03 \pm 0.03 \text{ } \mu\text{g C m}^{-3}$. For comparison, at Zeppelin and Villum the annual mean EC concentrations were $0.012 \pm 0.04 \text{ } \mu\text{g C m}^{-3}$ (2017-2020) (Yttri et al., 2024) and $0.029 \pm 0.03 \text{ } \mu\text{g C m}^{-3}$ (2011-2013) (Massling et al., 2015), respectively.

Annual mean OC concentrations during the entire study period were estimated as $0.45 \pm 0.3 \text{ } \mu\text{g C m}^{-3}$. At Zeppelin, annual OC (2017-2020) was 3.5 smaller ($0.13 \pm 0.1 \text{ } \mu\text{g C m}^{-3}$) (Yttri et al., 2024). Notably, the multi-year average EC and OC levels at IBS are approximately 3 times higher than at Zeppelin, that correlates well with increased light absorption, as described previously. At IBS, OC was $0.4 \pm 0.2 \text{ } \mu\text{g C m}^{-3}$ in the cold period and increased to $0.5 \pm 0.4 \text{ } \mu\text{g C m}^{-3}$ in warm period, opposite

363 to EC (**Table 1**). The ratio OC/EC shows increased OC and decreased EC in the warm period and
 364 an opposite trend in the cold (**Figure 4b**). **Figure 4c** depicts the relationship between eBC_{AET} and
 365 EC in cold and warm periods. We note the high R^2 values for the cold period (0.88) and slightly
 366 lower ones for the warm one (0.78). During the warm period, seasonal mean values reveal an
 367 overestimation of eBC_{AET} that is more pronounced during the warm period, with a slope equal to
 368 2.3. R^2 values were lower because many EC values were close to the LOD. Seasonal differences are
 369 attributed to pollutant sources altering the chemical composition of aerosol at IBS. A positive
 370 correlation was observed between eBC_{AET}/EC and OC/EC indicating that BC at IBS is coated with
 371 OC leading to the lens effect (Kanaya et al., 2008) and overestimating eBC .

372 Similar seasonal variation for eBC and EC with highest winter and lower summer
 373 concentrations has been observed previously at Villum, with a regression slope of 2 and a R^2 of
 374 0.64 (Massling et al., 2015). At Alert, the median SAC during the Arctic haze season (November to
 375 April) was $19.8 \text{ m}^2 \text{ g}^{-1}$ (Sharma et al., 2004). However, during the non-Arctic haze period from May
 376 to October it was significantly higher $28.8 \text{ m}^2 \text{ g}^{-1}$ and much more variable. This is explained by
 377 aged, internally mixed, and of anthropogenic origin of winter and spring arctic aerosols while
 378 summer aerosols were affected by local sources.

379 Following the definition in Eq.5, we calculate the SAC from the slope of BC light absorption
 380 at 880 nm, $b_{abs/BC}(880)$, and EC concentrations. $SAC_{BC,cold}$ (for the cold period) was estimated to
 381 be $15.9 \text{ m}^2 \text{ g}^{-1}$ while $SAC_{BC,warm}$ was higher ($18.1 \text{ m}^2 \text{ g}^{-1}$) (**Figure 5**). SAC values at Alert have
 382 been reported to be even higher (Sharma et al., 2004), showing that Western Arctic aerosols differ
 383 by composition and aging. Recalculations of BC mass with SAC values for cold and warm periods
 384 (eBC), separately, were performed according to Eq.1.

385 Timeseries of daily and monthly mean eBC concentrations from August 2019 to 31 December
 386 2022 are shown in **Figure 2**. Annual mean and median eBC for the entire period were 28.7 ± 54.1
 387 ngm^{-3} and 12.5 ng m^{-3} , respectively (**Table 1**); they exhibit a strong year-by-year variability. We
 388 note that the eBC values are approximately half of the eBC_{AET} value. Previous studies have
 389 evaluated the optical properties of BC against direct mass measurements techniques and also
 390 obtained MAC values depended on the location, different from the recommended by aethalometer
 391 (Sharma et al., 2004; Eleftheriadis et al., 2009; Yttri et al., 2024). For example, the relationship
 392 between BC_{AET} and EC obtained by the thermal technique at Alert station (Canada) during 3 - year
 393 measurements was 0.85 (Sharma et al., 2004). Studies at Villum Research Station (Greenland)
 394 showed good agreement between measured EC and eBC_{AET} concentrations (Massling et al., 2015)
 395 similar to our study. eBC climatology and the statistics for each month and year of study are

presented in **Figure 2** and **Table S 2**, respectively. The annual mean *eBC* in 2019, 2021 and 2022 was 33 ± 44 , 33 ± 85 , and 32 ± 48 ng m⁻³, respectively, for the entire study period. Statistically significant difference at the 95% confidence level (p-value <0.05, t-test) was observed for the cold and warm periods with means of 44 ± 47 and 19 ± 57 ng m⁻³, respectively. The smallest mean *eBC* of 24 ± 29 ng m⁻³ occurred in 2020. The latter is likely attributed to the impact of COVID-19 restriction measures to the emissions of BC (Evangeliou et al., 2020).

The general trend of the maximum in winter and minimum in summer well reproduces the typical *eBC* seasonality reported in polar observatories (Stone et al., 2014; Schmale et al., 2022). **Figure 2** shows monthly mean *eBC* concentrations for half of year 2019 and whole - year periods of 2020, 2021, and 2022 as well as annual averaged monthly mean *eBC* climatology for the entire study period. The highest concentration in the cold period was observed in December 2019 (81 ± 64 ng m⁻³), January 2022 (61 ± 49 ng m⁻³), February 2022 (106 ± 67 ng m⁻³), and March 2021 (42 ± 33 ng m⁻³) (**Table S 2**). In warm periods we recorded the highest concentrations in September 2020 (31 ± 48 ng m⁻³), August 2021 (83 ± 249 ng m⁻³), April 2021 (35 ± 26 ng m⁻³), and August 2022 (28 ± 54 ng m⁻³).

3.3 Multi-wavelength absorption Angstrom exponent

As shown by Virkkula (2021), pure BC particles surrounded by non-absorbing coatings can have *AAE* in the range from <1 to 1.7. Compendium of values from different emissions show *AAE* variation from 0.2 to 3.0 for transport, power plants, and domestic wood burning (Helin et al., 2021). Primary emissions from residential heating (Cuesta-Mosquera et al., 2024) and BB (Popovicheva et al., 2017a, 2019b) have been associated with high *AAE* of around 3-4. Due to the mixing with background aerosol, coating and aging processes, a large change in the light absorption has been reported at receptors of long-range transported pollution (Cappa et al., 2016). For highly aged aerosols, *AAE* has been found lower than 1.0 due to large and internally mixed particles (Popovicheva et al., 2022). Spectral absorption was obtained at IBS in the UV to IR spectral region emphasized by the value of $AAE_{350/950}$ equal to 0.96 for the entire study period (**Figure 6a**). Power law fittings of spectral dependence for both and cold periods show similar values, indicating highly mixed and aged BC.

Multiple studies have addressed the sensitivity of the *AAE* to the range of wavelengths selected for its calculation (Cuesta-Mosquera et al., 2024); the extent of this sensitivity is higher for aerosols containing a substantial contribution of organic species such as BrC. Events affected by regional fire emissions were evident by the light absorption coefficient $AAE_{370/520}$ in the short wavelength range (Ulevicius et al., 2010). In remote Arctic environments, cases with exceeded $AAE_{467/660}$ have been identified to be influenced by BB (Pulimeno et al., 2024). Impact of

intensive wildfires in North America on aerosol optical properties measured at the European Arctic has been associated with increased daily $AAE_{467/660}$ of up to 1.4 (Markowicz et al., 2016). Strong UV absorption has led to increase of up to 1.8, clearly indicating the importance of non-BC light-absorbing component (Ran et al., 2016).

To apportion the wavelength-dependent light absorption, we used a pair of wavelengths (350 and 950 nm) in the whole spectrum, and in shorter wavelengths (370 and 660 nm, 370 and 520 nm). Timeseries of weekly average $AAE_{370/520}$ showed a similar seasonality but wider variation (0.2-3.1) than (0.5-1.7) for $AAE_{370/950}$ (**Figure 6b**). The mean values increased from 0.97 ± 0.23 for $AAE_{370/950}$ to 1.17 ± 0.5 for $AAE_{370/520}$ for the entire study period (**Table 1**). Box-whisker plots and annual averaged means of $AAE_{370/950}$ showed no prominent monthly dependence (**Figure 4c**). However, increased $AAE_{370/950}$ above 1.1 was observed in summer months for several years, in July 2020, June 2021 and from May to September 2022 (**Table S 2**). The shorter the wavelength pair, the higher the annual average AAE above 1.0. The largest values of monthly mean (median) $AAE_{370/520}$ were found for April to September with a maximum in June. Such considerable deviation during warm months implies the importance of BrC light-absorbing components within highly mixed Arctic aerosols at IBS.

Light absorption at 370 nm, $b_{abs}(370)$, was used to estimate the BrC mass concentrations. The mean (median) value of $b_{abs}(370)$ was 2.4 times higher than $b_{abs}(880)$ for the entire study period as well as for cold and warm ones (**Table 1**). Monthly means and box-whisker plot of $b_{abs}(370)$ showed trends similar to $b_{abs}(880)$ (**Figure S 4**). Assuming that the wavelength pair λ and λ_0 in Eq. 3 being 370 and 950 nm, respectively, the absorption coefficient for BrC at 370 nm, $b_{abs/BrC}(370)$, is determined by subtracting BC absorption from the total absorption at the same wavelength using the $AAE_{370/950}$ value for entire period (**Table 1**). Monthly $b_{abs/BrC}(370)$ and $b_{abs/BrC}(370)$ as well as the $b_{abs/BrC}(370)$ percentage contribution to total $b_{abs}(370)$ are shown in **Table S 3** for those years when the contribution of BrC absorption was higher than 1%. We note 13% for August 2021 for the warm period and 5 % for February 2022 and December 2021 for the cold period.

3.4 Modelled concentrations of BC

Figure 7a shows the monthly mean eBC and surface BC ($BC_{FLEXPART}$) concentrations simulated with FLEXPART coupled to ECLIPSEv6-GFAS emissions for the entire study period. FLEXPART model performs well in capturing the seasonality of observed features with both high and low concentrations. Annual mean modelled $BC_{FLEXPART}$ (88.4 ng m^{-3}) is 37% higher than eBC_{AET} (64.3 ng m^{-3}) and 3 times higher than eBC (29.5 ng m^{-3}). Annual and monthly means of

463 eBC_{AET} show values closer to $BC_{FLEXPART}$ than eBC . This is a reasonable finding because the
464 global emission datasets could not consider local pollution. Almost all simulated BC
465 concentrations, except in February 2020 and 2021, were found within the standard deviation range
466 of measured eBC_{AET} . A good correlation between measurements and simulations, with a Pearson
467 coefficient of 0.72 and 0.82, a root mean squared error (RMSE) of 15 ng m⁻³ and 0.14 ng m⁻³ and a
468 normalised bias of 0.39 and 0.27 was obtained for the cold and warm period, respectively (**Figure**
469 **7b,c**).

470 FLEXPART does not reproduce seasonal variations of BC everywhere over the Arctic. R²
471 and RMSE varied between 0.53-0.80 and 15.1-56.8 ng m⁻³, respectively, depending on the location
472 (Zhu et al., 2020). At Zeppelin, modelled BC (annual mean of 39.1 ng m⁻³) was reported to be 85%
473 higher than the measured value (21.1 ng m⁻³ for annual mean). At Tiksi, modelled BC was
474 underestimated (74.4 ng m⁻³ for annual mean) by 40% compared with observations (104.2 ng m⁻³ for
475 annual mean) (Zhu et al., 2020). Such good result for IBS is due to its closer location to the biggest
476 emission sources.

477 **Figure 8** shows the vertical distribution of simulated BC as a function of time for 2019-2020
478 years (vertical cross-section). Consistently high vertical BC profiles up to 2 km were observed in
479 the cold period, except in April 2022. In February 2020, a smoke layer of BC concentrations of up
480 to 100 ng m⁻³ was prominent at up to 4 km. On the contrary, in the warm period the smoke resides
481 near the surface, despite a few events of extremely high vertical BC at altitudes up to 8 km and 10
482 km, which occurred in July 2020 and August 2021, respectively. Nevertheless, the evidence of
483 atmospheric transport from high altitudes during summer months is evident by the elevated
484 modelled BC (>100 ng m⁻³) at high model layers (e.g., July 2019, June-August 2020, June-July
485 2021 and May-June 2022). In all these periods, $BC_{FLEXPART}$ (gray line in **Figure 8**) was under 40 ng
486 m⁻³ showing that the emission sources are probably far away, and that long-range transport
487 occurred. The low injection altitude of anthropogenic emissions in winter months cause emitted
488 substances to remain close to the emission sources. BC climatology at IBS indicates that the long-
489 range transported anthropogenic emissions in the cold period reside at altitudes up to 2 km and
490 compose a persistent layer (**Figure 8**). This is further explained by the rapid (about 4 days, or less)
491 low-level transport of air masses to the Arctic troposphere as described in Stohl (2006). However,
492 this cannot be confirmed without targeted high altitude observations.

493 **4 Discussion**

494 **4.1 Long-range transport, age and region contributions**

495 Transport mechanisms from the source regions affect the Arctic BC variability and burden
496 (Chen et al., 2023; Zhou et al., 2012). Transport of aerosols to the Arctic leads to high
497 concentrations of BC in winter and spring (Arctic haze) and low values in summer (Law and Stohl,
498 2007) when the removal processes in the dry and stable Arctic atmosphere are very slow. Synoptic-
499 scale circulation effects promote the effective transport from lower latitudes, namely diabatic
500 cooling of air masses moving over snow-covered ground, high continental pressure in winter, and
501 the intrusion of warm air from lower latitudes (Gilardoni et al., 2023). Seasonal trends of footprint
502 emission sensitivity demonstrate the transport mechanisms from the source regions to the European
503 Arctic (Platt et al., 2021). BC at Zeppelin is affected by significantly different source regions during
504 the warm and cold seasons, while large-scale circulation patterns that affect the pollutant transport
505 from lower latitudes show the opposite behaviour during these two periods (Stathopoulos et al.,
506 2021).

507 **Figure 9** shows a 3.5-year climatology of the surface footprint emission sensitivities at IBS.
508 From December to February, anthropogenic polluted air mass transportation takes place from
509 Eurasia (territories above 40°N), as illustrated by the elevated footprints there. The extension of the
510 Arctic front towards lower latitudes during the cold period facilitates such transport (Stohl, 2006).
511 The warmer it gets in spring, the narrower the area of emission transport. In the transition from
512 spring to summer, transport patterns and meteorological conditions change, such as that the
513 advection of the particulate pollution to the Arctic boundary layer from lower latitudes becomes
514 limited (Bozem et al., 2019). In JJA (June, July, August) footprint is mostly restricted to coastal
515 regions of Eurasia, Greenland, and North America and does not extend deeply into the continents.
516 This is a consequence of the so-called ‘polar dome’ that prevents warm continental air masses from
517 entering the Arctic lower troposphere (Stohl, 2006). As a result, anthropogenic pollution becomes
518 less significant, and natural aerosol sources prevail (Moschos et al., 2022b, a). In autumn
519 (September, October, November), footprint is similar to the MAM (March, April, May) one
520 completing the annual cycle.

521 For the entire study period, the monthly mean contribution to surface BC for all years was
522 from air masses with 1-3 (31%) and 3-6 days (22%) aging (**Table S 4**). The highest BC contribution
523 (34%) and (39%) was observed for the shortest age of 1-3 days in DJF (December, January,
524 February) and MAM, respectively (**Figure 8**). In summer, the highest BC contribution (35%) was
525 replaced by a longer age of 6-9 days.

Footprint emission sensitivities of Arctic air masses also constrain the region contributions. The major source regions contributing BC to IBS are the territory of the Russian Federation (including European part of Russia (EURus), Siberia, Far East), Asia, Europe, Northern America, and Ocean. Due to the geographical proximity, EURus/Siberia/Far East contribution (77%) dominated during the entire study period on a basis of the annual average monthly means (**Table S 4**), with a maximum of 83% in SON (**Figure 9**). Its monthly maximum (88%) was recorded in September 2021, and the minimum (60%) in June 2022. Europe was the second region contributor (11%) followed by Asia. The monthly mean contribution of Northern America was up to 12% in JJA, the largest was observed in July 2022 (62%).

4.2 Anthropogenic and biomass burning sources

The time series of monthly mean and annual average monthly mean source contributions to surface BC at IBS are shown in **Figure 10a**. Anthropogenic sources (DOM, TRA, IND, FLR, All others) contribute 97% of the total for the entire study period (Table S 4). A decrease from winter to July and an increase from August to winter were seen. In the cold period, air masses arrived at IBS through the populated regions of Western Europe, EURus, Siberia, and Asia, crossing the biggest oil and gas extraction regions of Kazakhstan, Volga-Ural, Komi, Nenets, and Western Siberia (Figure 1). Because IBS is located north of the largest oil and gas producing regions of Western Siberia, high FLR contribution of 59% and 32% was observed both in the cold and warm period (Table S 4). Annual mean contributions to modelled surface BC from FLR, DOM, TRA, and IND sectors dominated in January and December (60%, 22%, 12%, and 9%, respectively). All other sources were around 2% at that time. BB played the biggest role between April (8%) and October (17%), with maximum in August (80%).

Figure S 5 shows the percentage sectoral contributions on monthly mean BC concentrations for 2021 and 2022, data for 2019 and 2020 was shown in Figure 10a. February 2021 and December 2021 were the leaders of FLR impact with 67.2% and 67.4%, respectively. During February 2022 of the record high BC pollution level observed at IBS, air masses arrived at IBS through the Western Europe, EURus, and Siberia, passing through the flaring facilities of Kazakhstan, Volga-Ural, Komi, Nenets, and Western Siberia. They caused of 50%, 26%, 15%, 8%, 0.2%, and 3.3% monthly average contribution to surface BC from FLR, DOM, TRA, IND, BB and All other sources, respectively. Footprint emission sensitivities on 3rd February 2022 at 12:00-15:00 when eBC reached 310 ng m⁻³ (Figure S 5) showed air mass transport to IBS straight through the Western Siberian gas flaring region (Figure 10b).

The contribution of FLR dropped significantly from April to a minimum of 18% in June and rose in September. In the winter months when the overestimation of modelled BC concentrations

560 was recorded (see section 3.4), the highest FLR impact was seen. DOM showed the biggest
561 contribution (18%) from November to February, exactly during the heating season. The light
562 absorption of BrC was significant mostly in wintertime (Table S 3). The latter indicates significant
563 impact of biomass used for domestic heating, in accordance to wood burning contribution of 61% of
564 the total residential emissions in forest regions (Huang et al., 2015).

565 According to CAMS GFAS (Figure S 3), significant global fire emissions started from June
566 and lasted until the mid of November in 2020 and 2022; the period of fire emissions was shorter but
567 more intensive from July until September 2021. At IBS, the annual mean BB contribution
568 approached 48% of the total in the warm season (Table S 4). It started increasing from April and
569 approached a maximum of 80% in August, whereas TRA, DOM, IND, and All other sources were
570 minimum. From middle June to September, the average monthly BB contribution was larger than
571 all anthropogenic sources. Notably, from April to September, the high mean BB contribution was
572 related to the excess of $AAE_{370/520}$ over 1.0 (maximum: 1.7 in July) (Figure 6). At that time, the air
573 masses transported to IBS were aged (> 6 days) dominating the age spectrum (57%) (Table S 4).

574 In 2019, 72,400 km² were burned in Siberia or 42% of the total burned area that occurred in
575 Russia (Voronova et al., 2020). A significant relationship between the burned areas and associated
576 pyrogenic emissions with atmospheric blocking events was reported (Mokhov et al., 2020). August
577 and September showed 50% and 35%, respectively, monthly mean BB contributions, while October
578 and November lower, 30% and 20%, respectively (Figure S4).

579 In spring 2020, BB BC concentrations simulated with WRF-Chem model were distributed in
580 areas between 40°N and 60°N in Europe, central Siberia, and East Asia, and indicated intensive
581 seasonal agriculture fires in Europe and Siberia (Chen et al., 2023). Spring fires contributed about
582 12% BB BC to IBS (April and May). The end of June and beginning of July of 2020 was
583 characterized by high altitude BC (Figure 8) indicating high altitude long-range transport. A high
584 BrC content was also observed in July and September 2020 (Table S 3).

585 In 2021, the monthly mean spring BB contribution approached a maximum of 36% in May.
586 Yakutia (Eastern Siberia) experienced the worst fire season over the last four decades (Tomshin and
587 Solovyev, 2022). Around 150,000 fires occurred, almost twice as much as the previous year
588 (Voronova et al., 2022). August 2021 received 90% contribution from BB as compared to all the
589 other sources. At that time unprecedented high smoke levels were recorded over Western Siberia
590 (Schneider et al., 2024). Satellite image reveals the strong plume from the area of Yakutian
591 wildfires which brought deep smoke to IBS located around 2000 km far away (Figure 1c). The
592 highest eBC level of 1800 ng m⁻³ on 5th August, exceeded the 75th percentile of the entire period

53 times (Table 1). The measured concentrations were 180 times higher than the Arctic background (Figure S 6). Severe smoke affected the visibility near IBS (Figure 1d). Footprint emission sensitivity on 5th August (from 18:00 to 21:00) at the time when *eBC* peaked (1540 ng m⁻³) confirms that air masses originated from Yakutia and arrived to IBS from the northeast direction (Figure 10b). BC for these wildfires was transported at altitude as high as 10 km (Figure 8). Finally, in summer 2022, wildfires took place in Western Siberia and the EURus (Popovicheva et al., 2023); BB contributions in June, July, August 2022 were around 65%, whereas light absorption of BrC was important in May and August 2022 (Table S 3).

5 Summary and conclusions

We presented four years (2019-2022) of observations at the aerosol station IBS with respect to light-absorption characteristics of Western Siberian polar aerosols and its basic cycles, such as seasonality, annual means, and interannual variability. The annual cycle of multi-wavelength light absorption demonstrates higher levels during the Arctic haze season and lower in summer, similar to other Arctic observations. The light absorption coefficient revealed several unique features:

Higher values of the light absorption coefficient (around 4-5 times) in comparison with multi-year observations at high-latitude polar stations in European Arctic (annual mean of 0.7 ± 0.7 M m⁻¹ in the cold season and 2 times lower in warm). Wintertime maximum was observed in February (0.9 ± 0.8 M m⁻¹) that coincides with the Arctic haze peak; this is different from the European and Canadian Arctic that is usually observed in early spring. The interannual minimum was observed in June whereas August was highly variable with respect to light-absorption due to the Siberian wildfires. Multi-annual monthly means for $b_{abs}(880)$ in the visible spectrum at IBS were found higher than at European, Canadian and Western high-latitude polar locations, due to that IBS is closer to the main Northern Eurasian source regions.

Wildfires caused increased concentrations, usually in August. Increase of the AAE in the UV spectrum between April and September implies coexistence of highly mixed/aged BC and light-absorbing BrC components. Specifically, monthly BrC contribution to total light absorption was 5% in February 2022 and 13% August 2021 likely due to wildfire impact. BrC light absorption coefficient in the UV spectrum showed similar trends as BC, although it exceeded BC by 2.4 times during both cold and warm periods. AAE was equal to 0.96, indicating highly mixed and aged aerosols. AAE in UV spectrum increase up to 1.17 ± 0.5 implies coexistence of light-absorbing BrC components in BB aerosols, with the biggest impact between April and September.

We calculated SAC for the first time at IBS by combining multi-year optical absorption and EC data. Higher SAC of 18.1 m² g⁻¹ in the warm period than in the cold one (15.9 m² g⁻¹) revealed

626 influence from non-BC light-absorbing species, such as organic matter and mineral dust; SAC
627 values were lower than those observed in the Canadian Arctic indicating different aerosol
628 composition and aging. Mean eBC in the cold and warm periods were equal to 44 ± 47 and 19 ± 57 ng
629 m^{-3} , respectively. Record high eBC was found in February 2022 (106 ± 67 ng m^{-3}) and August 2021
630 (83 ± 249 ng m^{-3}) during the years of study.

631 Observations at the IBS station evaluated the relationship between eBC_{AET} and EC under
632 specific atmospheric conditions. eBC , recalculated using site-specific absorption coefficients,
633 reflects seasonal variations and provides insights into aerosol composition. Annual cycles follow
634 typical Arctic trends, with higher eBC concentrations in winter when air masses primarily originate
635 from Russia, Siberia, the Far East, Europe, and Asia. During this period, black carbon from gas
636 flaring dominates, particularly in January, when air masses pass over oil and gas facilities in
637 Kazakhstan, Volga-Ural, Komi, Nenets, and Western Siberia. In summer, biomass burning (BB)
638 from Siberian wildfires surpasses anthropogenic sources, peaking in August 2021, which saw the
639 worst fire season in four decades, bringing heavy smoke to IBS. February 2022 also recorded
640 extreme BC pollution levels.

641 Modeling analyses indicate that 77% of BC transport originated from Russia, Siberia, and
642 the Far East, followed by Europe (11%), Asia (7%), and North America (4%). In winter, air masses
643 traveled 1-3 days from Eurasia (north of $40^{\circ}N$) to IBS, whereas in summer, transport took 6-9 days.
644 Low-injection altitude anthropogenic emissions created a persistent BC layer up to 2 km in the cold
645 season, reaching 4 km in February 2020, with record concentrations of 100 ng m^{-3} . In contrast,
646 wildfire smoke in summer elevated BC layers to higher altitudes.

647 Anthropogenic emissions accounted for 83% of BC during the study period, dominated by
648 gas flaring (FLR, 59%), domestic heating (DOM, 18%), traffic (TRA, 10%), and industry (IND,
649 7%) during Arctic haze period. Gas flaring remained the primary contributor year-round (59% in
650 winter, 32% in summer), given IBS's proximity to major oil and gas regions. Residential heating
651 peaked in winter (18%), aligning with enhanced brown carbon (BrC) absorption from wood
652 burning. In February 2022, modeled BC concentrations reached 310 ng m^{-3} as air masses passed
653 through major flaring regions, though overestimation suggests miscalculated source intensities.

654 BB contributions peaked at 48% in the warm season, surpassing anthropogenic sources from
655 mid-June to September, with a maximum of 80% in August. Extreme vertical BC events reached 8
656 km in July 2020 and 10 km in August 2021 due to wildfires. In May 2021, BB contributions
657 reached 36% due to strong agricultural fires in Siberia, while in August 2021, 90% of BC at IBS
658 originated from Yakutia's wildfires, 2000 km away.

659 The increasing intensity and frequency of wildfires at high latitudes highlight the importance
660 of carbonaceous aerosol measurements. These observations provide critical insights into Arctic

661 aerosol radiative properties, particularly in the UV-VIS spectrum, where enhanced light absorption
662 contributes to amplified Arctic warming, especially in summer.

663
664

665 **Data availability.** All modelling data from this study are available for download from [https://atmo-](https://atmo-access.nilu.no/BELY2_MSU.py)
666 [access.nilu.no/BELY2_MSU.py](https://atmo-access.nilu.no/BELY2_MSU.py). FLEXPART version 10.4 model can be downloaded from
667 <https://www.flexpart.eu/downloads>. Black Carbon observations are available upon request from O.
668 B. Popovicheva.

669

670 **Supplement.** The supplement related to this article is available online at.

671

672 **Author contributions.** OBP supervised the station operation, interpreted data and wrote the
673 manuscript. NE performed all the FLEXPART simulations and analyses, wrote and coordinated the
674 paper. MAC analysed the data, prepared the figures and assisted in the interpretation of the results.
675 ED provided supported *AAE* calculations and evaluation of data quality. NSK supported the
676 research. All authors contributed to the final version of the manuscript.

677

678 **Competing interests.** The authors declare no competing interests.

679

680 **Acknowledgements.** This research was performed in the frame of the development program of the
681 Interdisciplinary Scientific and Educational School of M. V. Lomonosov Moscow State University
682 (MSU) “Future Planet and Global Environmental Change”. For instrument calibration, the
683 equipment of MSU Shared Research Equipment Center “Technologies for obtaining new
684 nanostructured materials and their complex study” was used. This equipment was purchased by
685 MSU in the frame of the Equipment Renovation Program (National Project “Science”). Authors
686 thank Magee Scientific for AE33 instrumentation support and Dr. Asta Gregorič for data
687 examination. V.O. Kobelev is acknowledged data analyses over all study years.

688

689 **Financial support.** The article processing charges for this publication were paid by NILU.
690 Developed methodology of aethalometric measurements was implemented in the frame of the RSF
691 project #19-77-3004П. Authors thanks to Russian Geographical Society for the data treatment
692 support Institute of Environmental Survey, Planning and Assessment (IESPA) partly supported the
693 instrumentation and power supply of IBS.

694

695 **References**

696 AMAP: AMAP assessment 2015: Black carbon and ozone as Arctic climate forcers, Arctic
697 Monitoring and Assessment Programme (AMAP), Oslo, Norway, 128 pp. pp., 2015.

698 AMAP: AMAP Arctic Climate Change Update 2021: Key Trends and Impacts,
699 <https://www.amap.no/documents/download/6759/inline>, 2021.

700 Arnold, S. R., Law, K. S., Brock, C. A., Thomas, J. L., Starkweather, S. M., Von Salzen, K., Stohl,
701 A., Sharma, S., Lund, M. T., Flanner, M. G., Petäjä, T., Tanimoto, H., Gamble, J., Dibb, J. E.,
702 Melamed, M., Johnson, N., Fidel, M., Tynkkynen, V. P., Baklanov, A., Eckhardt, S., Monks, S. A.,
703 Browse, J., and Bozem, H.: Arctic air pollution: Challenges and opportunities for the next decade,
704 *Elementa*, 2016, 1–17, <https://doi.org/10.12952/journal.elementa.000104>, 2016.

705 Asmi, E., Kivekäs, N., Kerminen, V. M., Komppula, M., Hyvärinen, A. P., Hatakka, J., Viisanen,
706 Y., and Lihavainen, H.: Secondary new particle formation in Northern Finland Pallas site between
707 the years 2000 and 2010, *Atmos. Chem. Phys.*, 11, 12959–12972, [https://doi.org/10.5194/acp-11-](https://doi.org/10.5194/acp-11-12959-2011)
708 12959-2011, 2011.

709 Asmi, E., Backman, J., Servomaa, H., Virkkula, A., Gini, M. I., Eleftheriadis, K., Müller, T., Ohata,
710 S., Kondo, Y., and Hyvärinen, A.: Absorption instruments inter-comparison campaign at the Arctic
711 Pallas station, *Atmos. Meas. Tech.*, 14, 5397–5413, <https://doi.org/10.5194/amt-14-5397-2021>,
712 2021.

713 Backman, J., Schmeisser, L., Virkkula, A., Ogren, J. A., Asmi, E., Starkweather, S., Sharma, S.,
714 Eleftheriadis, K., Uttal, T., Jefferson, A., Bergin, M., Makshtas, A., Tunved, P., and Fiebig, M.: On
715 Aethalometer measurement uncertainties and an instrument correction factor for the Arctic, *Atmos.*
716 *Meas. Tech.*, 10, 5039–5062, <https://doi.org/10.5194/amt-10-5039-2017>, 2017.

717 Bali, K., Banerji, S., Campbell, J. R., Bhakta, A. V., Chen, L. W. A., Holmes, C. D., and Mao, J.:
718 Measurements of brown carbon and its optical properties from boreal forest fires in Alaska summer,
719 *Atmos. Environ.*, 324, 120436, <https://doi.org/10.1016/j.atmosenv.2024.120436>, 2024.

720 Bond, T. C., Doherty, S. J., Fahey, D. W., Forster, P. M., Berntsen, T., Deangelo, B. J., Flanner, M.
721 G., Ghan, S., Kärcher, B., Koch, D., Kinne, S., Kondo, Y., Quinn, P. K., Sarofim, M. C., Schultz,
722 M. G., Schulz, M., Venkataraman, C., Zhang, H., Zhang, S., Bellouin, N., Guttikunda, S. K.,
723 Hopke, P. K., Jacobson, M. Z., Kaiser, J. W., Klimont, Z., Lohmann, U., Schwarz, J. P., Shindell,
724 D., Storelvmo, T., Warren, S. G., and Zender, C. S.: Bounding the role of black carbon in the
725 climate system: A scientific assessment, *J. Geophys. Res. Atmos.*, 118, 5380–5552,
726 <https://doi.org/10.1002/jgrd.50171>, 2013.

727 Bondur, V. G., Voronova, O. S., Cherepanova, E. V., Tsidilina, M. N., and Zima, A. L.:
728 Spatiotemporal Analysis of Multi-Year Wildfires and Emissions of Trace Gases and Aerosols in
729 Russia Based on Satellite Data, *Izv. - Atmos. Ocean Phys.*, 56, 1457–1469,
730 <https://doi.org/10.1134/S0001433820120348>, 2020.

731 Böttcher, K., Paunu, V.-V., Kupiainen, K., Zhizhin, M., Matveev, A., Savolahti, M., Klimont, Z.,
 732 Väättäin, S., Lamberg, H., and Karvosenoja, N.: Black carbon emissions from flaring in Russia in
 733 the period 2012-2017, *Atmos. Environ.*, 254, 118390,
 734 <https://doi.org/10.1016/j.atmosenv.2021.118390>, 2021.

735 Bozem, H., Hoor, P., Kunkel, D., Köllner, F., Schneider, J., Herber, A., Schulz, H., Richard
 736 Leaitch, W., Aliabadi, A. A., Willis, M. D., Burkart, J., and Abbatt, J. P. D.: Characterization of
 737 transport regimes and the polar dome during Arctic spring and summer using in situ aircraft
 738 measurements, *Atmos. Chem. Phys.*, 19, 15049–15071, <https://doi.org/10.5194/acp-19-15049-2019>,
 739 2019.

740 Cappa, C. D., Kolesar, K. R., Zhang, X., Atkinson, D. B., Pekour, M. S., Zaveri, R. A., Zelenyuk,
 741 A., and Zhang, Q.: Understanding the optical properties of ambient sub-and supermicron particulate
 742 matter: Results from the CARES 2010 field study in northern California, *Atmos. Chem. Phys.*, 16,
 743 6511–6535, <https://doi.org/10.5194/acp-16-6511-2016>, 2016.

744 Cassiani, M., Stohl, A., and Brioude, J.: Lagrangian Stochastic Modelling of Dispersion in the
 745 Convective Boundary Layer with Skewed Turbulence Conditions and a Vertical Density Gradient:
 746 Formulation and Implementation in the FLEXPART Model, *Boundary-Layer Meteorol.*, 154, 367–
 747 390, <https://doi.org/10.1007/s10546-014-9976-5>, 2015.

748 Chakrabarty, R. K., Moosmüller, H., Chen, L. W. A., Lewis, K., Arnott, W. P., Mazzoleni, C.,
 749 Dubey, M. K., Wold, C. E., Hao, W. M., and Kreidenweis, S. M.: Brown carbon in tar balls from
 750 smoldering biomass combustion, *Atmos. Chem. Phys.*, 10, 6363–6370, [https://doi.org/10.5194/acp-](https://doi.org/10.5194/acp-10-6363-2010)
 751 10-6363-2010, 2010.

752 Chen, X., Kang, S., Yang, J., and Hu, Y.: Contributions of biomass burning in 2019 and 2020 to
 753 Arctic black carbon and its transport pathways, *Atmos. Res.*, 296, 107069,
 754 <https://doi.org/10.1016/j.atmosres.2023.107069>, 2023.

755 Cuesta-Mosquera, A., Glojek, K., Močnik, G., Drinovec, L., Gregorič, A., Rigler, M., Ogrin, M.,
 756 Romshoo, B., Weinhold, K., Merkel, M., Van Pinxteren, D., Herrmann, H., Wiedensohler, A.,
 757 Pöhlker, M., and Müller, T.: Optical properties and simple forcing efficiency of the organic aerosols
 758 and black carbon emitted by residential wood burning in rural central Europe, *Atmos. Chem. Phys.*,
 759 24, 2583–2605, <https://doi.org/10.5194/acp-24-2583-2024>, 2024.

760 Drinovec, L., Močnik, G., Zotter, P., Prévôt, A. S. H., Ruckstuhl, C., Coz, E., Rupakheti, M.,
 761 Sciare, J., Müller, T., Wiedensohler, A., and Hansen, A. D. A.: The “dual-spot” Aethalometer: An
 762 improved measurement of aerosol black carbon with real-time loading compensation, *Atmos. Meas.*
 763 *Tech.*, 8, 1965–1979, <https://doi.org/10.5194/amt-8-1965-2015>, 2015.

764 Eleftheriadis, K., Vratolis, S., and Nyeki, S.: Aerosol black carbon in the European Arctic:
 765 Measurements at Zeppelin station, Ny-Ålesund, Svalbard from 1998-2007, *Geophys. Res. Lett.*, 36,

1–5, <https://doi.org/10.1029/2008GL035741>, 2009.

Evangeliou, N., Balkanski, Y., Hao, W. M., Petkov, A., Silverstein, R. P., Corley, R., Nordgren, B. L., Urbanski, S. P., Eckhardt, S., Stohl, A., Tunved, P., Crepinsek, S., Jefferson, A., Sharma, S., Nøjgaard, J. K., and Skov, H.: Wildfires in northern Eurasia affect the budget of black carbon in the Arctic—a 12-year retrospective synopsis (2002–2013), *Atmos. Chem. Phys.*, 16, <https://doi.org/10.5194/acp-16-7587-2016>, 2016.

Evangeliou, N., Platt, S., Eckhardt, S., Lund Myhre, C., Laj, P., Alados-Arboledas, L., Backman, J., Brem, B., Fiebig, M., Flentje, H., Marinoni, A., Pandolfi, M., Yus-Diez, J., Prats, N., Putaud, J., Sellegri, K., Sorribas, M., Eleftheriadis, K., Vratolis, S., Wiedensohler, A., and Stohl, A.: Changes in black carbon emissions over Europe due to COVID-19 lockdowns, *Atmos. Chem. Phys.*, 1–33, <https://doi.org/10.5194/acp-2020-1005>, 2020.

Flanner, M. G.: Arctic climate sensitivity to local black carbon, *J. Geophys. Res. Atmos.*, 118, 1840–1851, <https://doi.org/10.1002/jgrd.50176>, 2013.

Forster, C., Stohl, A., and Seibert, P.: Parameterization of convective transport in a Lagrangian particle dispersion model and its evaluation, *J. Appl. Meteorol. Climatol.*, 46, 403–422, <https://doi.org/10.1175/JAM2470.1>, 2007.

Gilardoni, S., Heslin-Rees, D., Mazzola, M., Vitale, V., Sprenger, M., and Krejci, R.: Drivers controlling black carbon temporal variability in the lower troposphere of the European Arctic, *Atmos. Chem. Phys.*, 23, 15589–15607, <https://doi.org/10.5194/acp-23-15589-2023>, 2023.

Gramlich, Y., Siegel, K., Haslett, S. L., Cremer, R. S., Lunder, C., Kommula, S. M., Buchholz, A., Yttri, K. E., Chen, G., Krejci, R., Zieger, P., Virtanen, A., Riipinen, I., and Mohr, C.: Impact of Biomass Burning on Arctic Aerosol Composition, <https://doi.org/10.1021/acsearthspacechem.3c00187>, 2024.

Grange, S. K., Lötscher, H., Fischer, A., Emmenegger, L., and Hueglin, C.: Evaluation of equivalent black carbon source apportionment using observations from Switzerland between 2008 and 2018, *Atmos. Meas. Tech.*, 13, 1867–1885, <https://doi.org/10.5194/amt-13-1867-2020>, 2020.

Grythe, H., Kristiansen, N. I., Groot Zwaaftink, C. D., Eckhardt, S., Ström, J., Tunved, P., Krejci, R., and Stohl, A.: A new aerosol wet removal scheme for the Lagrangian particle model FLEXPARTv10, *Geosci. Model Dev.*, 10, 1447–1466, <https://doi.org/10.5194/gmd-10-1447-2017>, 2017.

Helin, A., Virkkula, A., Backman, J., Pirjola, L., Sippula, O., Aakko-Saksa, P., Väättäinen, S., Mylläri, F., Järvinen, A., Bloss, M., Aurela, M., Jakobi, G., Karjalainen, P., Zimmermann, R., Jokiniemi, J., Saarikoski, S., Tissari, J., Rönkkö, T., Niemi, J. V., and Timonen, H.: Variation of Absorption Ångström Exponent in Aerosols From Different Emission Sources, *J. Geophys. Res. Atmos.*, 126, 1–21, <https://doi.org/10.1029/2020JD034094>, 2021.

801 Hersbach, H., Bell, B., Berrisford, P., Hirahara, S., Horányi, A., Muñoz-Sabater, J., Nicolas, J.,
 802 Peubey, C., Radu, R., Schepers, D., Simmons, A., Soci, C., Abdalla, S., Abellan, X., Balsamo, G.,
 803 Bechtold, P., Biavati, G., Bidlot, J., Bonavita, M., De Chiara, G., Dahlgren, P., Dee, D.,
 804 Diamantakis, M., Dragani, R., Flemming, J., Forbes, R., Fuentes, M., Geer, A., Haimberger, L.,
 805 Healy, S., Hogan, R. J., Hólm, E., Janisková, M., Keeley, S., Laloyaux, P., Lopez, P., Lupu, C.,
 806 Radnoti, G., de Rosnay, P., Rozum, I., Vamborg, F., Villaume, S., and Thépaut, J. N.: The ERA5
 807 global reanalysis, *Q. J. R. Meteorol. Soc.*, 146, 1999–2049, <https://doi.org/10.1002/qj.3803>, 2020.
 808 Heslin-Rees, D., Burgos, M., Hansson, H. C., Krejci, R., Ström, J., Tunved, P., and Zieger, P.: From
 809 a polar to a marine environment: Has the changing Arctic led to a shift in aerosol light scattering
 810 properties?, *Atmos. Chem. Phys.*, 20, 13671–13686, <https://doi.org/10.5194/acp-20-13671-2020>,
 811 2020.
 812 Huang, K., Fu, J. S., Prikhodko, V. Y., Storey, J. M., Romanov, A., Hodson, E. L., Cresko, J.,
 813 Morozova, I., Ignatieva, Y., and Cabaniss, J.: Russian anthropogenic black carbon: Emission
 814 reconstruction and Arctic black carbon simulation, *J. Geophys. Res. Atmos.*, 120, 11306–11333,
 815 <https://doi.org/10.1002/2015JD023358>, 2015.
 816 Ivančič, M., Gregorič, A., Lavrič, G., Alföldy, B., Ježek, I., Hasheminassab, S., Pakbin, P.,
 817 Ahangar, F., Sowlat, M., Boddeker, S., and Rigler, M.: Two-year-long high-time-resolution
 818 apportionment of primary and secondary carbonaceous aerosols in the Los Angeles Basin using an
 819 advanced total carbon–black carbon (TC-BC(λ)) method, *Sci. Total Environ.*, 848,
 820 <https://doi.org/10.1016/j.scitotenv.2022.157606>, 2022.
 821 Johnson, M. S., Strawbridge, K., Knowland, K. E., Keller, C., and Travis, M.: Long-range transport
 822 of Siberian biomass burning emissions to North America during FIREX-AQ, *Atmos. Environ.*, 252,
 823 118241, <https://doi.org/10.1016/j.atmosenv.2021.118241>, 2021.
 824 Kaiser, J. W., Heil, A., Andreae, M. O., Benedetti, A., Chubarova, N., Jones, L., Morcrette, J. J.,
 825 Razinger, M., Schultz, M. G., Suttie, M., and Van Der Werf, G. R.: Biomass burning emissions
 826 estimated with a global fire assimilation system based on observed fire radiative power,
 827 *Biogeosciences*, 9, 527–554, <https://doi.org/10.5194/bg-9-527-2012>, 2012.
 828 Kanaya, Y., Komazaki, Y., Pochanart, P., Liu, Y., Akimoto, H., Gao, J., Wang, T., and Wang, Z.:
 829 Mass concentrations of black carbon measured by four instruments in the middle of Central East
 830 China in June 2006, *Atmos. Chem. Phys.*, 8, 7637–7649, <https://doi.org/10.5194/acp-8-7637-2008>,
 831 2008.
 832 Kasischke, E. S. and Turetsky, M. R.: Recent changes in the fire regime across the North American
 833 boreal region - Spatial and temporal patterns of burning across Canada and Alaska, *Geophys. Res.*
 834 *Lett.*, 33, <https://doi.org/10.1029/2006GL025677>, 2006.
 835 Kharuk, V. I. and Ponomarev, E. I.: Spatiotemporal characteristics of wildfire frequency and

relative area burned in larch-dominated forests of Central Siberia, *Russ. J. Ecol.*, 48, 507–512, <https://doi.org/10.1134/S1067413617060042>, 2017.

Klimont, Z., Kupiainen, K., Heyes, C., Purohit, P., Cofala, J., Rafaj, P., Borken-Kleefeld, J., and Schöpp, W.: Global anthropogenic emissions of particulate matter including black carbon, *Atmos. Chem. Phys.*, 17, 8681–8723, <https://doi.org/10.5194/acp-17-508681-2017>, 2017.

Kostrykin, S., Revokatova, A., Chernenkov, A., Ginzburg, V., Polumieva, P., and Zelenova, M.: Black carbon emissions from the siberian fires 2019: Modelling of the atmospheric transport and possible impact on the radiation balance in the arctic region, *Atmosphere (Basel)*, 12, <https://doi.org/10.3390/atmos12070814>, 2021.

Law, K. S. and Stohl, A.: Arctic Air Pollution: Origins and Impacts, *Science (80-.)*, 315, 1537–1540, <https://doi.org/10.1126/science.1137695>, 2007.

Lee, Y. H., Lamarque, J. F., Flanner, M. G., Jiao, C., Shindell, D. T., Berntsen, T., Bisiaux, M. M., Cao, J., Collins, W. J., Curran, M., Edwards, R., Faluvegi, G., Ghan, S., Horowitz, L., McConnell, J. R., Ming, J., Myhre, G., Nagashima, T., Naik, V., Rumbold, S. T., Skeie, R. B., Sudo, K., Takemura, T., Thevenon, F., Xu, B., and Yoon, J. H.: Evaluation of preindustrial to present-day black carbon and its albedo forcing from Atmospheric Chemistry and Climate Model Intercomparison Project (ACCMIP), *Atmos. Chem. Phys.*, 13, 2607–2634, <https://doi.org/10.5194/acp-13-2607-2013>, 2013.

Manousakas, M., Popovicheva, O., Evangeliou, N., Diapouli, E., Sitnikov, N., Shonija, N., and Eleftheriadis, K.: Aerosol carbonaceous, elemental and ionic composition variability and origin at the Siberian High Arctic, Cape Baranova, *Tellus B Chem. Phys. Meteorol.*, 72, 1–14, <https://doi.org/10.1080/16000889.2020.1803708>, 2020.

Markowicz, K. M., Pakszys, P., Ritter, C., Zielinski, T., Udisti, R., Cappelletti, D., Mazzola, M., Shiobara, M., Xian, P., Zawadzka, O., Lisok, J., Petelski, T., Makuch, P., and Karasinski, G.: Impact of North American intense fires on aerosol optical properties measured over the European Arctic in July 2015, *J. Geophys. Res.*, 121, 14487–14512, <https://doi.org/10.1002/2016JD025310>, 2016.

Massling, A., Nielsen, I. E., Kristensen, D., Christensen, J. H., Sorensen, L. L., Jensen, B., Nguyen, Q. T., Nøjgaard, J. K., Glasius, M., and Skov, H.: Atmospheric black carbon and sulfate concentrations in Northeast Greenland, *Atmos. Chem. Phys.*, 15, 9681–9692, <https://doi.org/10.5194/acp-15-9681-2015>, 2015.

Matsui, H., Mori, T., Ohata, S., Moteki, N., Oshima, N., Goto-Azuma, K., Koike, M., and Kondo, Y.: Contrasting source contributions of Arctic black carbon to atmospheric concentrations, deposition flux, and atmospheric and snow radiative effects, *Atmos. Chem. Phys.*, 22, 8989–9009, <https://doi.org/10.5194/acp-22-8989-2022>, 2022.

871 Mokhov, I. I., Bondur, V. G., Sitnov, S. A., and Voronova, O. S.: Satellite Monitoring of Wildfires
872 and Emissions into the Atmosphere of Combustion Products in Russia: Relation to Atmospheric
873 Blockings, *Dokl. Earth Sci.*, 495, 921–924, <https://doi.org/10.1134/S1028334X20120089>, 2020.

874 Moschos, V., Schmale, J., Aas, W., Becagli, S., Calzolari, G., Eleftheriadis, K., Moffett, C. E.,
875 Schnelle-Kreis, J., Severi, M., Sharma, S., Skov, H., Vestenius, M., Zhang, W., Hakola, H., Hellén,
876 H., Huang, L., Jaffrezo, J. L., Massling, A., Nøjgaard, J. K., Petäjä, T., Popovicheva, O., Sheesley,
877 R. J., Traversi, R., Yttri, K. E., Prévôt, A. S. H., Baltensperger, U., and El Haddad, I.: Elucidating
878 the present-day chemical composition, seasonality and source regions of climate-relevant aerosols
879 across the Arctic land surface, *Environ. Res. Lett.*, 17, <https://doi.org/10.1088/1748-9326/ac444b>,
880 2022a.

881 Moschos, V., Dzepina, K., Bhattu, D., Lamkaddam, H., Casotto, R., Daellenbach, K. R., Canonaco,
882 F., Rai, P., Aas, W., Becagli, S., Calzolari, G., Eleftheriadis, K., Moffett, C. E., Schnelle-Kreis, J.,
883 Severi, M., Sharma, S., Skov, H., Vestenius, M., Zhang, W., Hakola, H., Hellén, H., Huang, L.,
884 Jaffrezo, J. L., Massling, A., Nøjgaard, J. K., Petäjä, T., Popovicheva, O., Sheesley, R. J., Traversi,
885 R., Yttri, K. E., Schmale, J., Prévôt, A. S. H., Baltensperger, U., and El Haddad, I.: Equal
886 abundance of summertime natural and wintertime anthropogenic Arctic organic aerosols, *Nat.*
887 *Geosci.*, 15, 196–202, <https://doi.org/10.1038/s41561-021-00891-1>, 2022b.

888 Ohata, S., Mori, T., Kondo, Y., Sharma, S., Hyvärinen, A., Andrews, E., Tunved, P., Asmi, E.,
889 Backman, J., Servomaa, H., Veber, D., Eleftheriadis, K., Vratolis, S., Krejci, R., Zieger, P., Koike,
890 M., Kanaya, Y., Yoshida, A., Moteki, N., Zhao, Y., Tobo, Y., Matsushita, J., and Oshima, N.:
891 Estimates of mass absorption cross sections of black carbon for filter-based absorption photometers
892 in the Arctic, *Atmos. Meas. Tech.*, 14, 6723–6748, <https://doi.org/10.5194/amt-14-6723-2021>,
893 2021.

894 Paris, J.-D., Stohl, A., Nédélec, P., Arshinov, M. Y., Panchenko, M. V., Shmargunov, V. P., Law,
895 K. S., Belan, B. D., and Ciais, P.: Wildfire smoke in the Siberian Arctic in summer: source
896 characterization and plume evolution from airborne measurements, *Atmos. Chem. Phys.*, 9, 9315–
897 9327, <https://doi.org/10.5194/acp-9-9315-2009>, 2009, 2009.

898 Petzold, A., Rasp, K., Weinzierl, B., Esselborn, M., Hamburger, T., Dörnbrack, A., Kandler, K.,
899 Schütz, L., Knippertz, P., Fiebig, M., and Virkkula, A.: Saharan dust absorption and refractive
900 index from aircraft-based observations during SAMUM 2006, *Tellus, Ser. B Chem. Phys.*
901 *Meteorol.*, 61, 118–130, <https://doi.org/10.1111/j.1600-0889.2008.00383.x>, 2009.

902 Petzold, A., Ogren, J. A., Fiebig, M., Laj, P., Li, S. M., Baltensperger, U., Holzer-Popp, T., Kinne,
903 S., Pappalardo, G., Sugimoto, N., Wehrli, C., Wiedensohler, A., and Zhang, X. Y.:
904 Recommendations for reporting black carbon measurements, *Atmos. Chem. Phys.*, 13, 8365–8379,
905 <https://doi.org/10.5194/acp-13-8365-2013>, 2013.

906 Pisso, I., Sollum, E., Grythe, H., Kristiansen, N. I., Cassiani, M., Eckhardt, S., Arnold, D., Morton,
 907 D., Thompson, R. L., Groot Zwaftink, C. D., Evangeliou, N., Sodemann, H., Haimberger, L.,
 908 Henne, S., Brunner, D., Burkhardt, J. F., Fouilloux, A., Brioude, J., Philipp, A., Seibert, P., and
 909 Stohl, A.: The Lagrangian particle dispersion model FLEXPART version 10.4, *Geosci. Model Dev.*,
 910 12, 4955–4997, <https://doi.org/10.5194/gmd-12-4955-2019>, 2019.
 911 Platt, S., Hov, Ø., Berg, T., Breivik, K., Eckhardt, S., Eleftheriadis, K., Evangeliou, N., Fiebig, M.,
 912 Fisher, R., Hansen, G., Hansson, H.-C., Heintzenberg, J., Hermansen, O., Heslin-Rees, D., Holmén,
 913 K., Hudson, S., Kallenborn, R., Krejci, R., Krognes, T., Larssen, S., Lowry, D., Lund Myhre, C.,
 914 Lunder, C., Nisbet, E., Nizetto, P., Park, K.-T., Pedersen, C., Aspö Pfaffhuber, K., Röckmann, T.,
 915 Schmidbauer, N., Solberg, S., Stohl, A., Ström, J., Svendby, T., Tunved, P., Tørnkvist, K., van der
 916 Veen, C., Vratolis, S., Yoon, Y. J., Yttri, K. E., Zieger, P., Aas, W., and Tørseth, K.: Atmospheric
 917 composition in the European Arctic and 30 years of the Zeppelin Observatory, Ny-Ålesund, *Atmos.*
 918 *Chem. Phys.*, 1–80, 2021.
 919 Popovicheva, O., Diapouli, E., Makshtas, A., Shonija, N., Manousakas, M., Saraga, D., Uttal, T.,
 920 and Eleftheriadis, K.: East Siberian Arctic background and black carbon polluted aerosols at HMO
 921 Tiksi, *Sci. Total Environ.*, 655, 924–938, <https://doi.org/10.1016/j.scitotenv.2018.11.165>, 2019a.
 922 Popovicheva, O. B., Shonija, N. K., Persiantseva, N., Timofeev, M., Diapouli, E., Eleftheriadis, K.,
 923 Borgese, L., and Nguyen, X. A.: Aerosol pollutants during agricultural biomass burning: A case
 924 study in Ba Vi Region in Hanoi, Vietnam, *Aerosol Air Qual. Res.*, 17, 2762–2779,
 925 <https://doi.org/10.4209/aaqr.2017.03.0111>, 2017a.
 926 Popovicheva, O. B., Evangeliou, N., Eleftheriadis, K., Kalogridis, A. C., Sitnikov, N., Eckhardt, S.,
 927 and Stohl, A.: Black Carbon Sources Constrained by Observations in the Russian High Arctic,
 928 *Environ. Sci. Technol.*, 51, <https://doi.org/10.1021/acs.est.6b05832>, 2017b.
 929 Popovicheva, O. B., Engling, G., Ku, I. T., Timofeev, M. A., and Shonija, N. K.: Aerosol emissions
 930 from long-lasting smoldering of boreal peatlands: Chemical composition, markers, and
 931 microstructure, *Aerosol Air Qual. Res.*, 19, 484–503, <https://doi.org/10.4209/aaqr.2018.08.0302>,
 932 2019b.
 933 Popovicheva, O. B., Evangeliou, N., Kobelev, V. O., Chichaeva, M. A., Eleftheriadis, K., Gregorič,
 934 A., and Kasimov, N. S.: Siberian Arctic black carbon: gas flaring and wildfire impact, *Atmos.*
 935 *Chem. Phys.*, 22, 5983–6000, <https://doi.org/10.5194/acp-22-5983-2022>, 2022.
 936 Popovicheva, O. B., Chichaeva, M. A., Kobelev, V. O., and Kasimov, N. S.: Black Carbon
 937 Seasonal Trends and Regional Sources on Bely Island (Arctic), *Atmos. Ocean. Opt.*, 36, 176–184,
 938 <https://doi.org/10.1134/S1024856023030090>, 2023.
 939 Pulimeno, S., Bruschi, F., Feltracco, M., Mazzola, M., Gilardoni, S., Crocchianti, S., Cappelletti,
 940 D., Gambaro, A., and Barbaro, E.: Investigating the Presence of Biomass Burning Events at Ny-Å

941 Lesund: Optical and Chemical Insights from Summer-Fall 2019, *Atmos. Environ.*, 320, 120336,
 942 <https://doi.org/10.1016/j.atmosenv.2024.120336>, 2024.

943 Qi, L. and Wang, S.: Sources of black carbon in the atmosphere and in snow in the Arctic, *Sci.*
 944 *Total Environ.*, 691, 442–454, <https://doi.org/10.1016/j.scitotenv.2019.07.073>, 2019.

945 Ran, L., Deng, Z. Z., Wang, P. C., and Xia, X. A.: Black carbon and wavelength-dependent aerosol
 946 absorption in the North China Plain based on two-year aethalometer measurements, *Atmos.*
 947 *Environ.*, 142, 132–144, <https://doi.org/10.1016/j.atmosenv.2016.07.014>, 2016.

948 Rogers, B. M., Balch, J. K., Goetz, S. J., Lehmann, C. E. R., and Turetsky, M.: Focus on changing
 949 fire regimes: interactions with climate, ecosystems, and society, *Environ. Res. Lett.*, 15,
 950 <https://doi.org/10.1088/1748-9326/ab6d3a>, 2020.

951 Sandradewi, J., Prévôt, A. S. H., Szidat, S., Perron, N., Alfarra, M. R., Lanz, V. A., Weingartner,
 952 E., and Baltensperger, U. R. S.: Using aerosol light absorption measurements for the quantitative
 953 determination of wood burning and traffic emission contribution to particulate matter, *Environ. Sci.*
 954 *Technol.*, 42, 3316–3323, <https://doi.org/10.1021/es702253m>, 2008.

955 Schmale, J., Zieger, P., and Ekman, A. M. L.: Aerosols in current and future Arctic climate, *Nat.*
 956 *Clim. Chang.*, 11, 95–105, <https://doi.org/10.1038/s41558-020-00969-5>, 2021.

957 Schmale, J., Sharma, S., Decesari, S., Pernov, J., Massling, A., Hansson, H. C., Von Salzen, K.,
 958 Skov, H., Andrews, E., Quinn, P. K., Upchurch, L. M., Eleftheriadis, K., Traversi, R., Gilardoni, S.,
 959 Mazzola, M., Laing, J., and Hopke, P.: Pan-Arctic seasonal cycles and long-term trends of aerosol
 960 properties from 10 observatories, *Atmos. Chem. Phys.*, 22, 3067–3096, [https://doi.org/10.5194/acp-](https://doi.org/10.5194/acp-22-3067-2022)
 961 [22-3067-2022](https://doi.org/10.5194/acp-22-3067-2022), 2022.

962 Schmeisser, L., Backman, J., Ogren, J. A., Andrews, E., Asmi, E., Starkweather, S., Uttal, T.,
 963 Fiebig, M., Sharma, S., Eleftheriadis, K., Vratolis, S., Bergin, M., Tunved, P., and Jefferson, A.:
 964 Seasonality of aerosol optical properties in the Arctic, *Atmos. Chem. Phys.*, 18, 11599–11622,
 965 <https://doi.org/10.5194/acp-18-11599-2018>, 2018.

966 Schneider, E., Czech, H., Popovicheva, O., Chichayeva, M., Kobelev, V., Kasimov, N., Minkina, T.,
 967 Rüger, C. P., and Zimmermann, R.: Mass spectrometric analysis of unprecedented high levels of
 968 carbonaceous aerosol particles long-range transported from wildfires in the Siberian Arctic, *Atmos.*
 969 *Chem. Phys.*, 24, 553–576, <https://doi.org/10.5194/acp-24-553-2024>, 2024.

970 Sharma, S., Lavoué, D., Chachier, H., Barrie, L. A., and Gong, S. L.: Long-term trends of the black
 971 carbon concentrations in the Canadian Arctic, *J. Geophys. Res. D Atmos.*, 109, 1–10,
 972 <https://doi.org/10.1029/2003JD004331>, 2004.

973 Sharma, S., Ishizawa, M., Chan, D., Lavoué, D., Andrews, E., Eleftheriadis, K., and Maksyutov, S.:
 974 16-year simulation of arctic black carbon: Transport, source contribution, and sensitivity analysis on
 975 deposition, *J. Geophys. Res. Atmos.*, 118, 943–964, <https://doi.org/10.1029/2012JD017774>, 2013.

976 Sharma, S., Richard Leaitch, W., Huang, L., Veber, D., Kolonjari, F., Zhang, W., Hanna, S. J.,
 977 Bertram, A. K., and Ogren, J. A.: An evaluation of three methods for measuring black carbon in
 978 Alert, Canada, *Atmos. Chem. Phys.*, 17, 15225–15243, <https://doi.org/10.5194/acp-17-15225-2017>,
 979 2017.
 980 Silver, B., Arnold, S. R., Reddington, C. L., Emmons, L. K., and Conibear, L.: Large transboundary
 981 health impact of Arctic wildfire smoke, *Commun. Earth Environ.*, 5,
 982 <https://doi.org/10.1038/s43247-024-01361-3>, 2024.
 983 Singh, M., Kondo, Y., Ohata, S., Mori, T., Oshima, N., Hyvärinen, A., Backman, J., Asmi, E.,
 984 Servomaa, H., Schnaiter, F. M., Andrews, E., Sharma, S., Eleftheriadis, K., Vratolis, S., Zhao, Y.,
 985 Koike, M., Moteki, N., and Sinha, P. R.: Mass absorption cross section of black carbon for
 986 Aethalometer in the Arctic, *Aerosol Sci. Technol.*, 58, 536–553,
 987 <https://doi.org/10.1080/02786826.2024.2316173>, 2024.
 988 Stathopoulos, V. K., Evangeliou, N., Stohl, A., Vratolis, S., Matsoukas, C., and Eleftheriadis, K.:
 989 Large Circulation Patterns Strongly Modulate Long-Term Variability of Arctic Black Carbon
 990 Levels and Areas of Origin, *Geophys. Res. Lett.*, 48, 1–10, <https://doi.org/10.1029/2021GL092876>,
 991 2021.
 992 Stohl, A.: Characteristics of atmospheric transport into the Arctic troposphere, *J. Geophys. Res.*
 993 *Atmos.*, 111, 1–17, <https://doi.org/10.1029/2005JD006888>, 2006.
 994 Stohl, A., Forster, C., Frank, A., Seibert, P., and Wotawa, G.: Technical note: The Lagrangian
 995 particle dispersion model FLEXPART version 6.2, *Atmos. Chem. Phys.*, 5, 2461–2474,
 996 <https://doi.org/10.5194/acp-5-2461-2005>, 2005.
 997 Stohl, A., Klimont, Z., Eckhardt, S., Kupiainen, K., Shevchenko, V. P., Kopeikin, V. M., and
 998 Novigatsky, A. N.: Black carbon in the Arctic: The underestimated role of gas flaring and
 999 residential combustion emissions, *Atmos. Chem. Phys.*, 13, 8833–8855,
 1000 <https://doi.org/10.5194/acp-13-8833-2013>, 2013.
 1001 Stone, R. S., Sharma, S., Herber, A., Eleftheriadis, K., and Nelson, D. W.: A characterization of
 1002 Arctic aerosols on the basis of aerosol optical depth and black carbon measurements, *Elem. Sci.*
 1003 *Anthr.*, 2, 1–22, <https://doi.org/10.12952/journal.elementa.000027>, 2014.
 1004 Therneau, T.: deming: Deming, Theil-Sen, Passing-Bablok and Total Least Squares Regression,
 1005 2024.
 1006 Tomshin, O. and Solovyev, V.: Features of the Extreme Fire Season of 2021 in Yakutia (Eastern
 1007 Siberia) and Heavy Air Pollution Caused by Biomass Burning, *Remote Sens.*, 14,
 1008 <https://doi.org/10.3390/rs14194980>, 2022.
 1009 Tunved, P., Ström, J., and Krejci, R.: Arctic aerosol life cycle: Linking aerosol size distributions
 1010 observed between 2000 and 2010 with air mass transport and precipitation at Zeppelin station, Ny-

1011 Ålesund, Svalbard, *Atmos. Chem. Phys.*, 13, 3643–3660, [https://doi.org/10.5194/acp-13-3643-](https://doi.org/10.5194/acp-13-3643-2013)
 1012 2013, 2013.

1013 Ulevicius, V., Byčenkienė, S., Remeikis, V., Garbaras, A., Kecorius, S., Andriejauskienė, J.,
 1014 Jasinevičienė, D., and Mocnik, G.: Characterization of pollution events in the East Baltic region
 1015 affected by regional biomass fire emissions, *Atmos. Res.*, 98, 190–200,
 1016 <https://doi.org/10.1016/j.atmosres.2010.03.021>, 2010.

1017 Veraverbeke, S., Rogers, B. M., Goulden, M. L., Jandt, R. R., Miller, C. E., Wiggins, E. B., and
 1018 Randerson, J. T.: Lightning as a major driver of recent large fire years in North American boreal
 1019 forests, *Nat. Clim. Chang.*, 7, 529–534, <https://doi.org/10.1038/nclimate3329>, 2017.

1020 Vinogradova, A. A. and Ivanova, Y. A.: Atmospheric Transport of Black Carbon to the Russian
 1021 Arctic from Different Sources: Winter and Summer 2000–2016, *Atmos. Ocean. Opt.*, 36, 758–766,
 1022 <https://doi.org/10.1134/S1024856023060222>, 2023.

1023 Virkkula, A.: Modeled source apportionment of black carbon particles coated with a light-scattering
 1024 shell, *Atmos. Meas. Tech.*, 14, 3707–3719, <https://doi.org/10.5194/amt-14-3707-2021>, 2021.

1025 Voronova, O. S., Zima, A. L., Kladov, V. L., and Cherepanova, E. V.: Anomalous Wildfires in
 1026 Siberia in Summer 2019, *Izv. - Atmos. Ocean Phys.*, 56, 1042–1052,
 1027 <https://doi.org/10.1134/S000143382009025X>, 2020.

1028 Voronova, O. S., Gordo, K. A., Zima, A. L., and Feoktistova, N. V.: Strong Wildfires in the
 1029 Russian Federation in 2021 Detected Using Satellite Data, *Izv. - Atmos. Ocean Phys.*, 58, 1065–
 1030 1076, <https://doi.org/10.1134/S0001433822090225>, 2022.

1031 Willis, M. D., Leaitch, W. R., and Abbatt, J. P. D.: Processes Controlling the Composition and
 1032 Abundance of Arctic Aerosol, *Rev. Geophys.*, 56, 621–671,
 1033 <https://doi.org/10.1029/2018RG000602>, 2018.

1034 Winiger, P., Andersson, A., Eckhardt, S., Stohl, A., Semiletov, I. P., Dudarev, O. V., Charkin, A.,
 1035 Shakhova, N., Klimont, Z., Heyes, C., and Gustafsson, Ö.: Siberian Arctic black carbon sources
 1036 constrained by model and observation, *Proc. Natl. Acad. Sci.*, 114, E1054–E1061,
 1037 <https://doi.org/10.1073/pnas.1613401114>, 2017.

1038 Winiger, P., Barrett, T. E., Sheesley, R. J., Huang, L., Sharma, S., Barrie, L. A., and Yttri, K. E.:
 1039 Source apportionment of circum-Arctic atmospheric black carbon from isotopes and modeling, *Sci.*
 1040 *Adv.*, 5, eaau8052, <https://doi.org/10.1126/sciadv.aau8052>, 2019.

1041 Yttri, K. E., Lund Myhre, C., Eckhardt, S., Fiebig, M., Dye, C., Hirdman, D., Ström, J., Klimont,
 1042 Z., and Stohl, A.: Quantifying black carbon from biomass burning by means of levoglucosan - A
 1043 one-year time series at the Arctic observatory Zeppelin, *Atmos. Chem. Phys.*, 14, 6427–6442,
 1044 <https://doi.org/10.5194/acp-14-6427-2014>, 2014.

1045 Yttri, K. E., Bäcklund, A., Conen, F., Eckhardt, S., Evangeliou, N., Fiebig, M., Kasper-Giebl, A.,

1046 Gold, A., Gundersen, H., Myhre, C. L., Platt, S. M., Simpson, D., Surratt, J. D., Szidat, S., Rauber,
1047 M., Torseth, K., Ytre-Eide, M. A., Zhang, Z., and Aas, W.: Composition and sources of
1048 carbonaceous aerosol in the European Arctic at Zeppelin Observatory, Svalbard, *Atmos. Chem.*
1049 *Phys.*, 24, 2731–2758, 2024.

1050 Yue, S., Zhu, J., Chen, S., Xie, Q., Li, W., Li, L., Ren, H., Su, S., Li, P., Ma, H., Fan, Y., Cheng, B.,
1051 Wu, L., Deng, J., Hu, W., Ren, L., Wei, L., Zhao, W., Tian, Y., Pan, X., Sun, Y., Wang, Z., Wu, F.,
1052 Liu, C. Q., Su, H., Penner, J. E., Pöschl, U., Andreae, M. O., Cheng, Y., and Fu, P.: Brown carbon
1053 from biomass burning imposes strong circum-Arctic warming, *One Earth*, 5, 293–304,
1054 <https://doi.org/10.1016/j.oneear.2022.02.006>, 2022.

1055 Zanatta, M., Laj, P., Gysel, M., Baltensperger, U., Vratolis, S., Eleftheriadis, K., Kondo, Y.,
1056 Dubuisson, P., Winiarek, V., Kazadzis, S., Tunved, P., and Jacobi, H. W.: Effects of mixing state on
1057 optical and radiative properties of black carbon in the European Arctic, *Atmos. Chem. Phys.*, 18,
1058 14037–14057, <https://doi.org/10.5194/acp-18-14037-2018>, 2018.

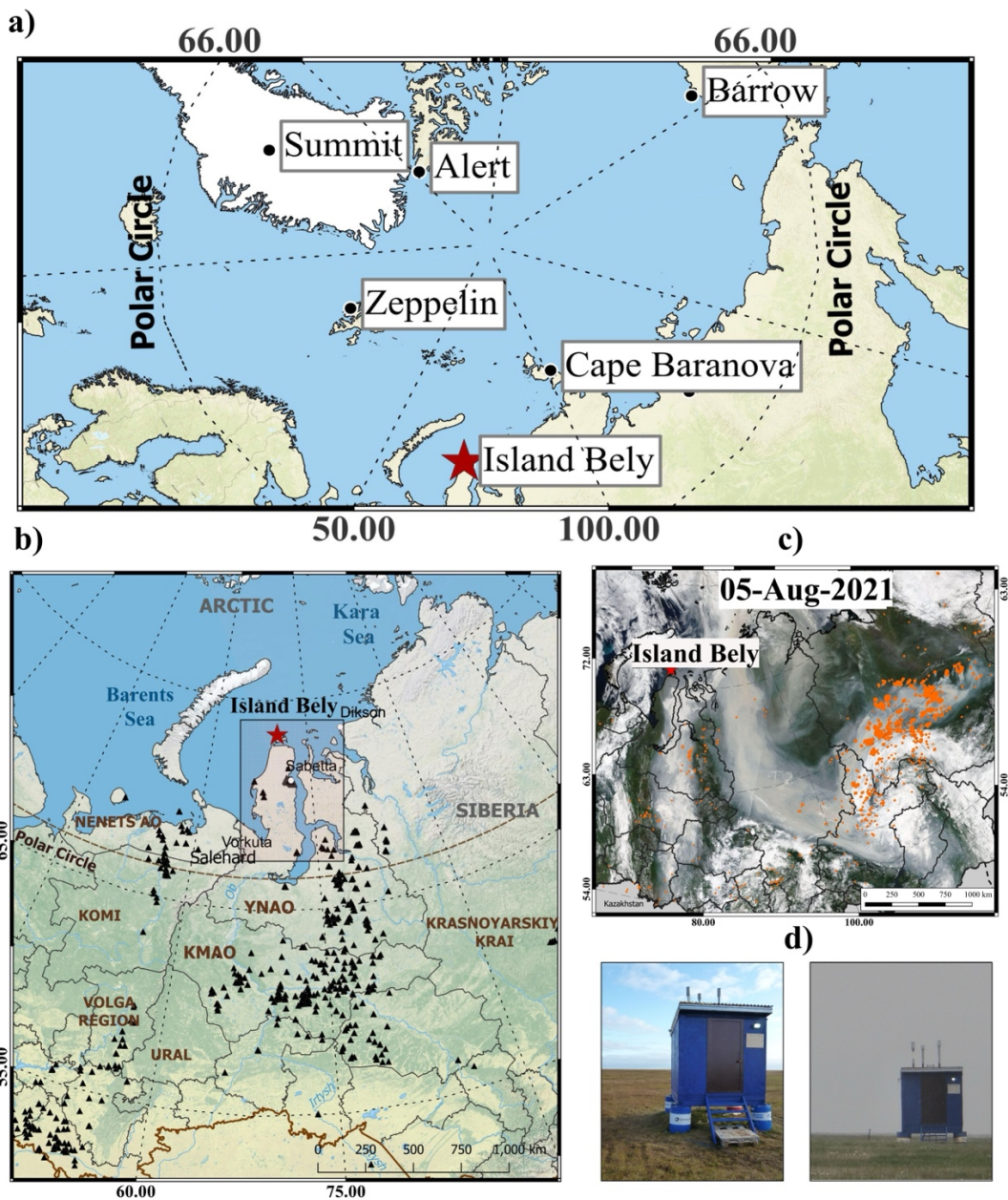
1059 Zenkova, P. N., Chernov, D. G., Shmargunov, V. P., Panchenko, M. V., and Belan, B. D.:
1060 Submicron Aerosol and Absorbing Substance in the Troposphere of the Russian Sector of the Arctic
1061 According to Measurements Onboard the Tu-134 Optik Aircraft Laboratory in 2020, *Atmos. Ocean.*
1062 *Opt.*, 35, 43–51, <https://doi.org/10.1134/S1024856022010146>, 2022.

1063 Zhou, C., Penner, J. E., Flanner, M. G., Bisiaux, M. M., Edwards, R., and McConnell, J. R.:
1064 Transport of black carbon to polar regions: Sensitivity and forcing by black carbon, *Geophys. Res.*
1065 *Lett.*, 39, 1–6, <https://doi.org/10.1029/2012GL053388>, 2012.

1066 Zhu, C., Kanaya, Y., Takigawa, M., Ikeda, K., Tanimoto, H., Taketani, F., Miyakawa, T.,
1067 Kobayashi, H., and Pissò, I.: FLEXPART v10.1 simulation of source contributions to Arctic black
1068 carbon, *Atmos. Chem. Phys.*, 20, 1641–1656, <https://doi.org/10.5194/acp-20-1641-2020>, 2020.

1069

1070



1073

1074 **Figure 1.** (a) The IBS between other polar aerosol stations. (b) A map showing IBS in Western
1075 Siberia along with oil and gas fields (adopted from <https://skytruth.org/>, last access: 7 November
1076 2024). Flares of oil and gas fields are indicated for 2020 as black triangles (<https://skytruth.org/>, last
1077 access: 7 November 2024). (c) Satellite image of strong plume from the area of Yakutian wildfires
1078 which brought deep smoke to the Bely Island. (d) View to the pavilion of IBS under clear
1079 conditions on 25 July 2021, and during the unprecedented smoke event on 5 August 2021. Maps
1080 were created using Open-Source Geographic Information System QGIS (<https://qgis.org/en/site>, last
1081 access: 7 November 2024) with ESRI physical imagery
1082 (https://server.arcgisonline.com/ArcGIS/rest/services/World_Physical_Map/MapServer/tile/%7Bz%7D/%7Bx%7D/%7By%7D/%7Bx%7D&zmax=20&zmin=0, last access: 7 November 2024) as the base layer,
1083 and for MODIS Reflectance true color imagery (MODIS Science Team) and Satellite imagery from
1084 05 of August 2021 (<https://worldview.earthdata.nasa.gov>, last access: 7 November 2024) with
1085 TERRA MODIS fire anomaly layer. Open-source Natural Earth quick start (NEQS) package was
1086 used to add layers of natural and cultural boundaries and polygons from ESRI Shapefile storage.
1087

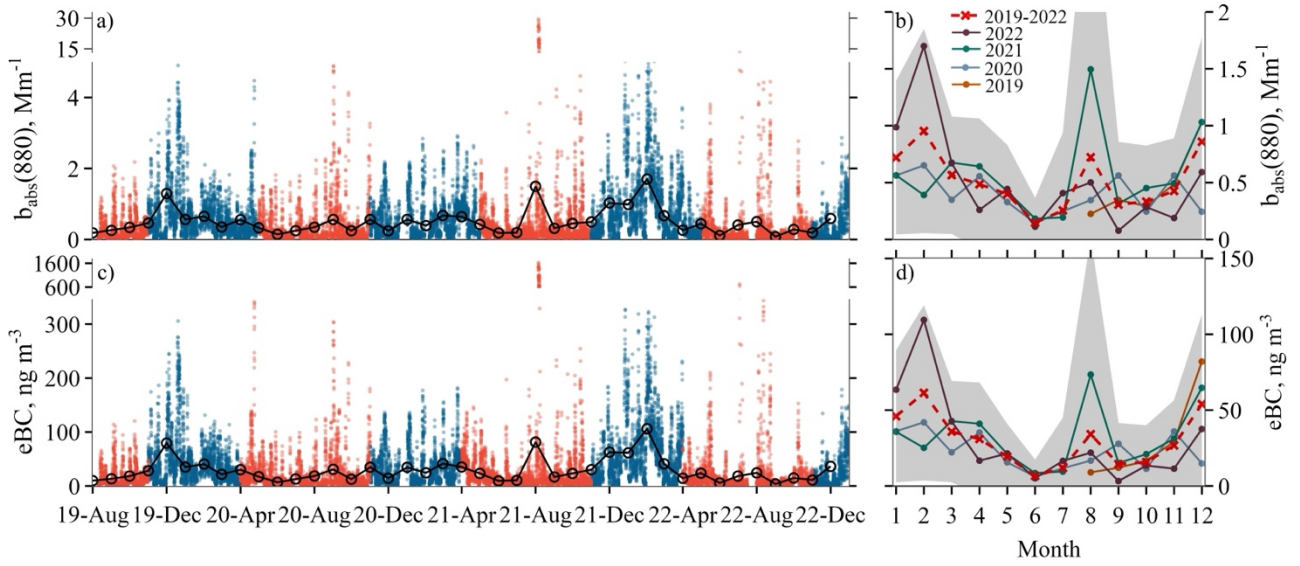
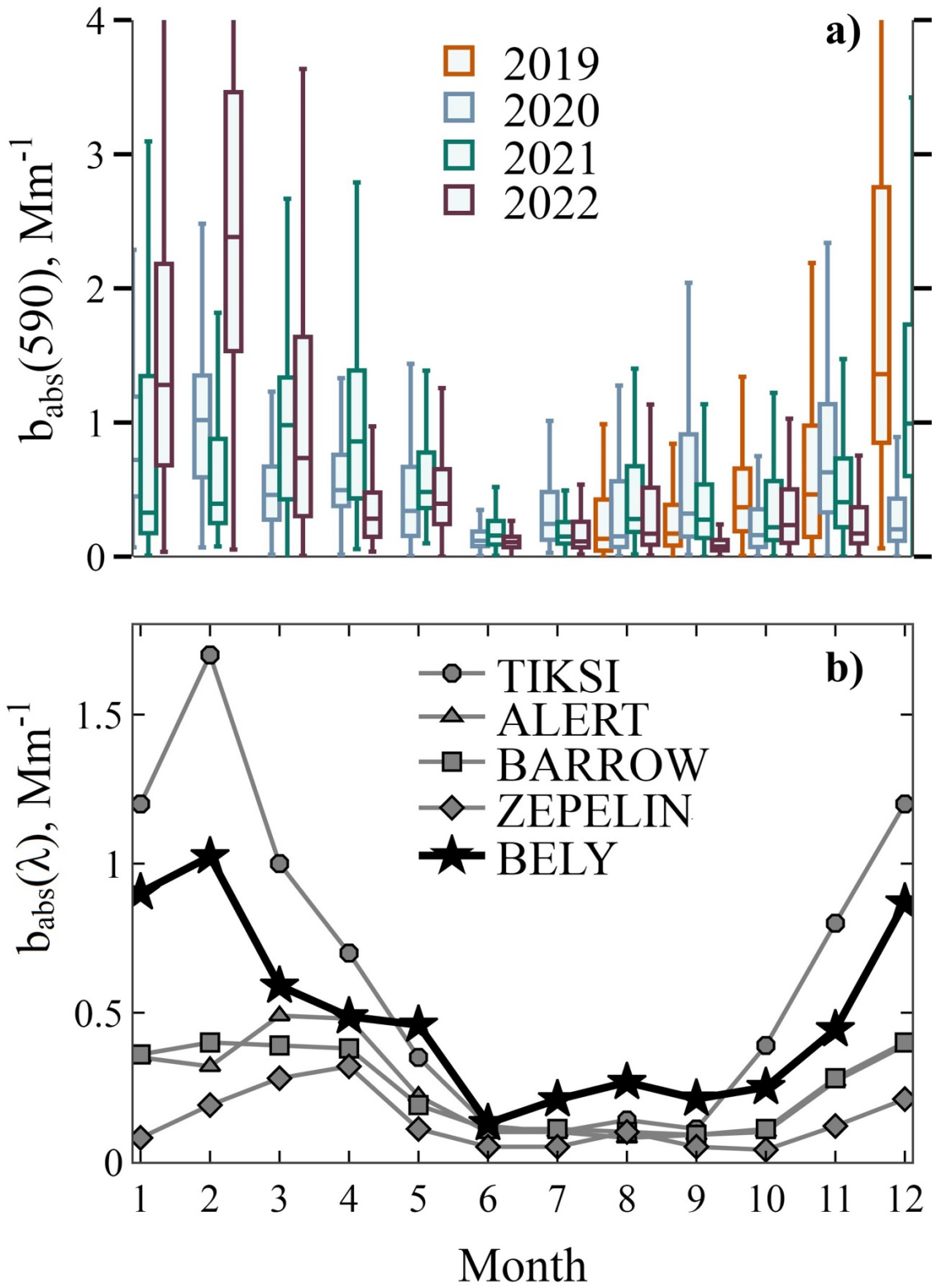
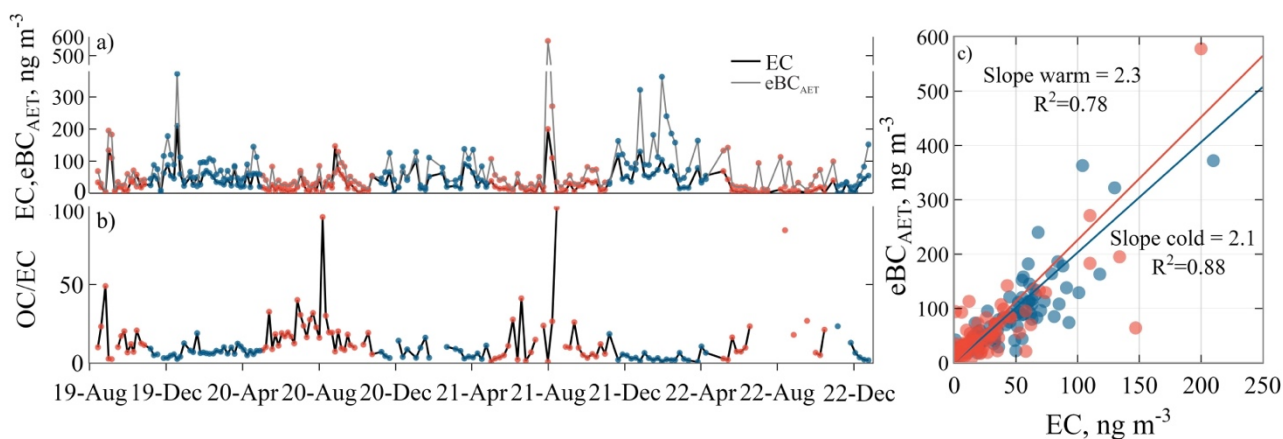


Figure 2. Hourly timeseries and monthly means of (a) $b_{abs}(880)$ and (c) eBC for cold (blue) and warm (red) periods; monthly climatology of (b) $b_{abs}(880)$ and (d) eBC for half year 2019 and 2020, 2021, and 2022. Cross-marks (x) joined by lines show the inter-annual mean; the standard deviation is plotted by shadow area.



1095

1096 **Figure 3.** (a) Monthly box-whisker plot for $b_{abs}(590)$ at IBS for half year 2019 and full 2020,
 1097 2021, and 2022. The 25th, 50th, and 75th percentiles are shown with boxes, while whiskers extend
 1098 ± 1.5 times the interquartile range. (b) Seasonality of monthly median of b_{abs} at 550 nm at Tiksi,
 1099 Alert, Barrow/Utqiagvik, Zepelin for 2012-2014 (Schmeisser et al., 2018), and b_{abs} at 590 nm at
 1100 IBS for 2019-2022 (this work).



1101

1102

1103

1104

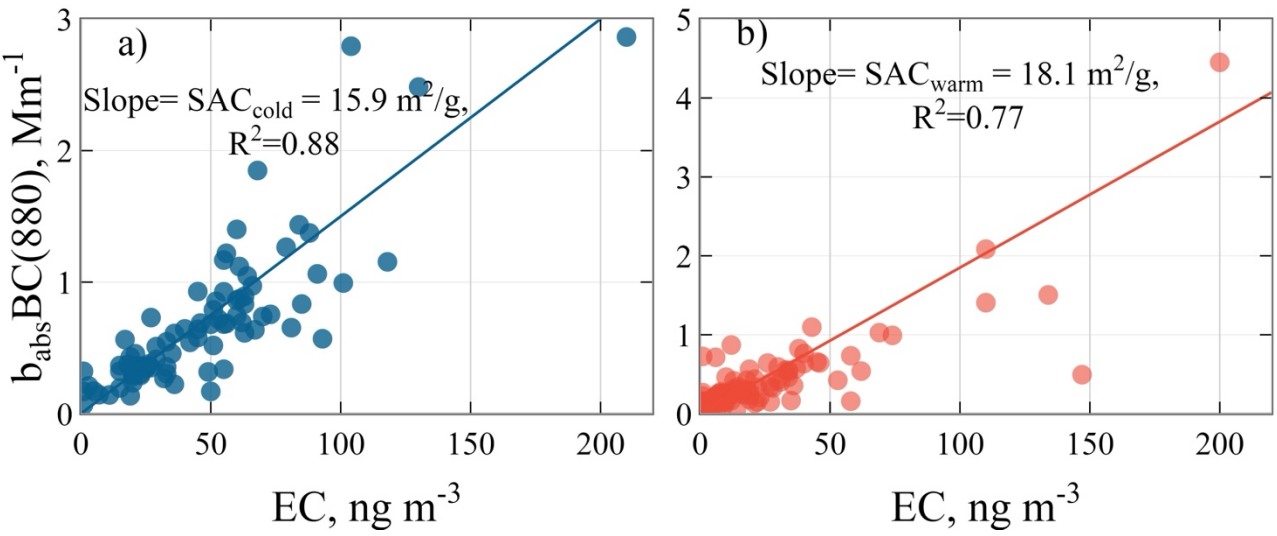
1105

1106

1107

Figure 4. Temporal variation of (a) weekly EC and eBC_{AET} averaged over the whole sampling period and (b) the OC/EC ratio. (c) Scatter plots and orthogonal regressions (solid lines) for measured eBC_{AET} and EC concentrations in cold (blue) and warm (red) period. The figure includes the regression slope, the coefficient of determination (R^2).

1108



1109

1110 **Figure 5.** Scatter plots and orthogonal regressions (solid line) for $b_{abs/BC}(880)$ and EC
1111 concentrations for the (a) cold (blue) and (b) warm (red) periods. Regression slope defines
1112 $SAC_{BC,cold}$ and $SAC_{BC,warm}$.

1113

1114

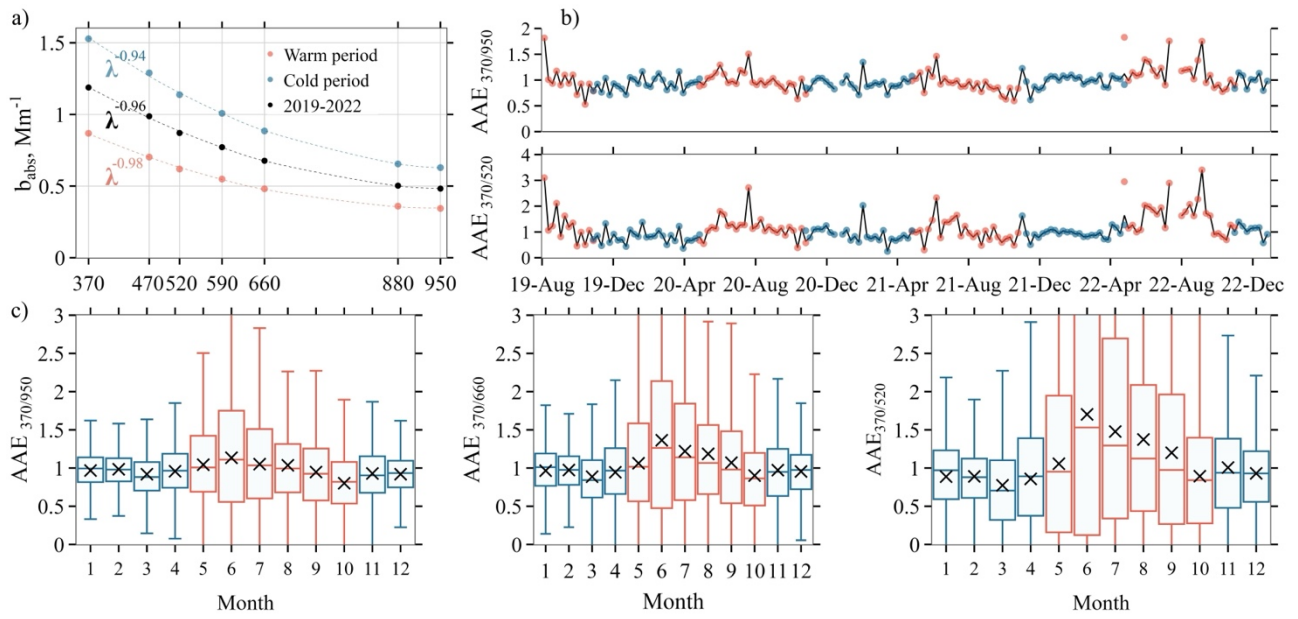
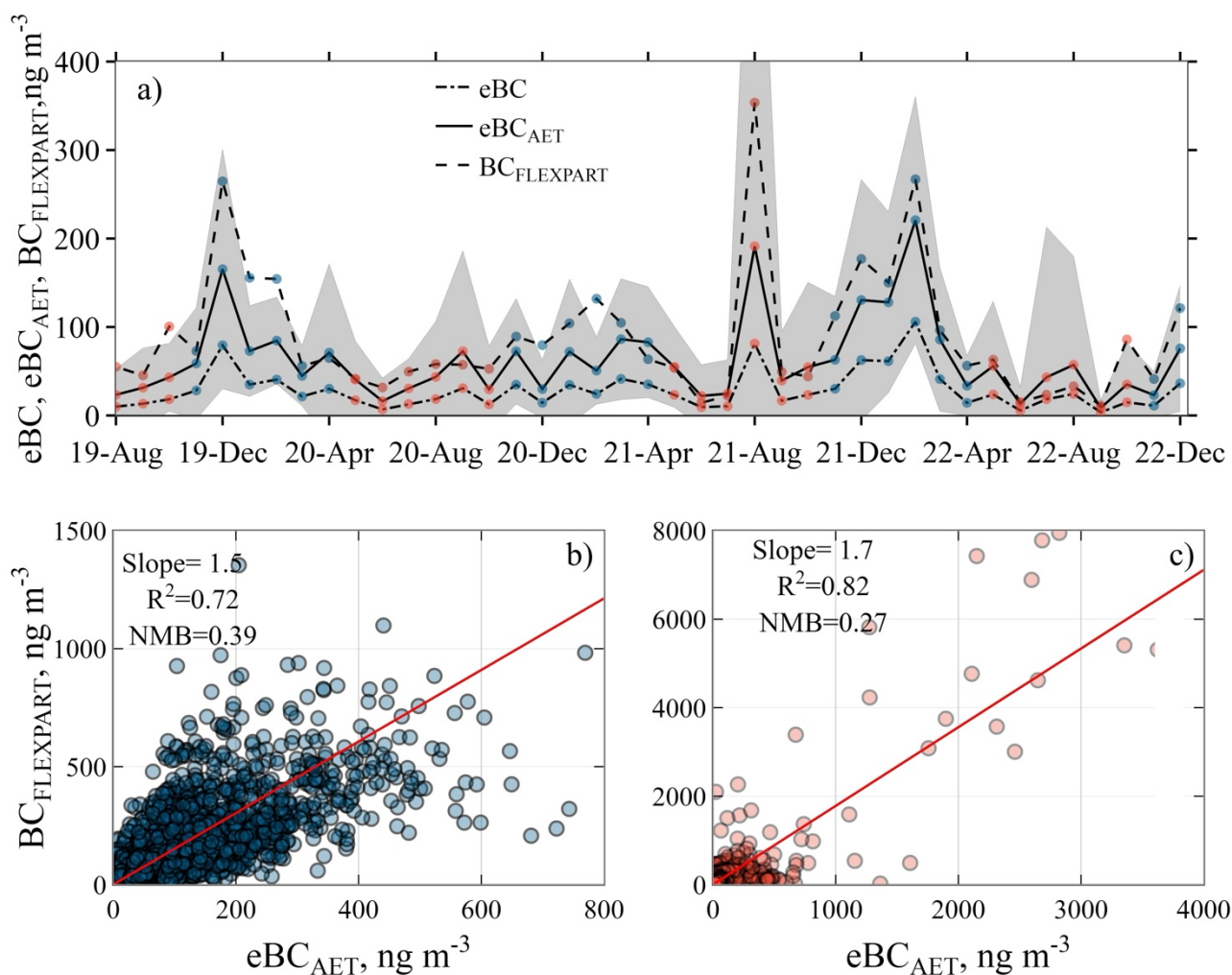


Figure 6. (a) Spectral dependence of light absorption coefficient for 2019-2022, during warm (red) and cold (blue) periods. $AAE_{370/950}$ is the slope of the linear regression in logarithmic scale of a power law regression as described in Eq. 2. (b) Timeseries of $AAE_{370/950}$ and $AAE_{370/520}$. (c) Box-whisker plots and monthly means of AAE at 370 and 950 nm, 370 and 660 nm, and 370 and 520 nm for the entire period.



1122

1123

1124

1125

1126

1127

1128

Figure 7. (a) Monthly mean eBC and modelled surface BC concentrations from 10 August 2019 to 31 December 2022. Monthly mean eBC_{AET} (line with crosses) shown with the standard deviation range by shadowed area. Scatter plots and orthogonal regressions (solid lines) for $BC_{FLEXPART}$ calculated over measured eBC_{AET} concentrations for (b) cold and (c) warm period. The figure includes the regression slope, the coefficient of determination (R^2).

VERTICAL CROSS-SECTIONS OF MODELLED BC IN IBS

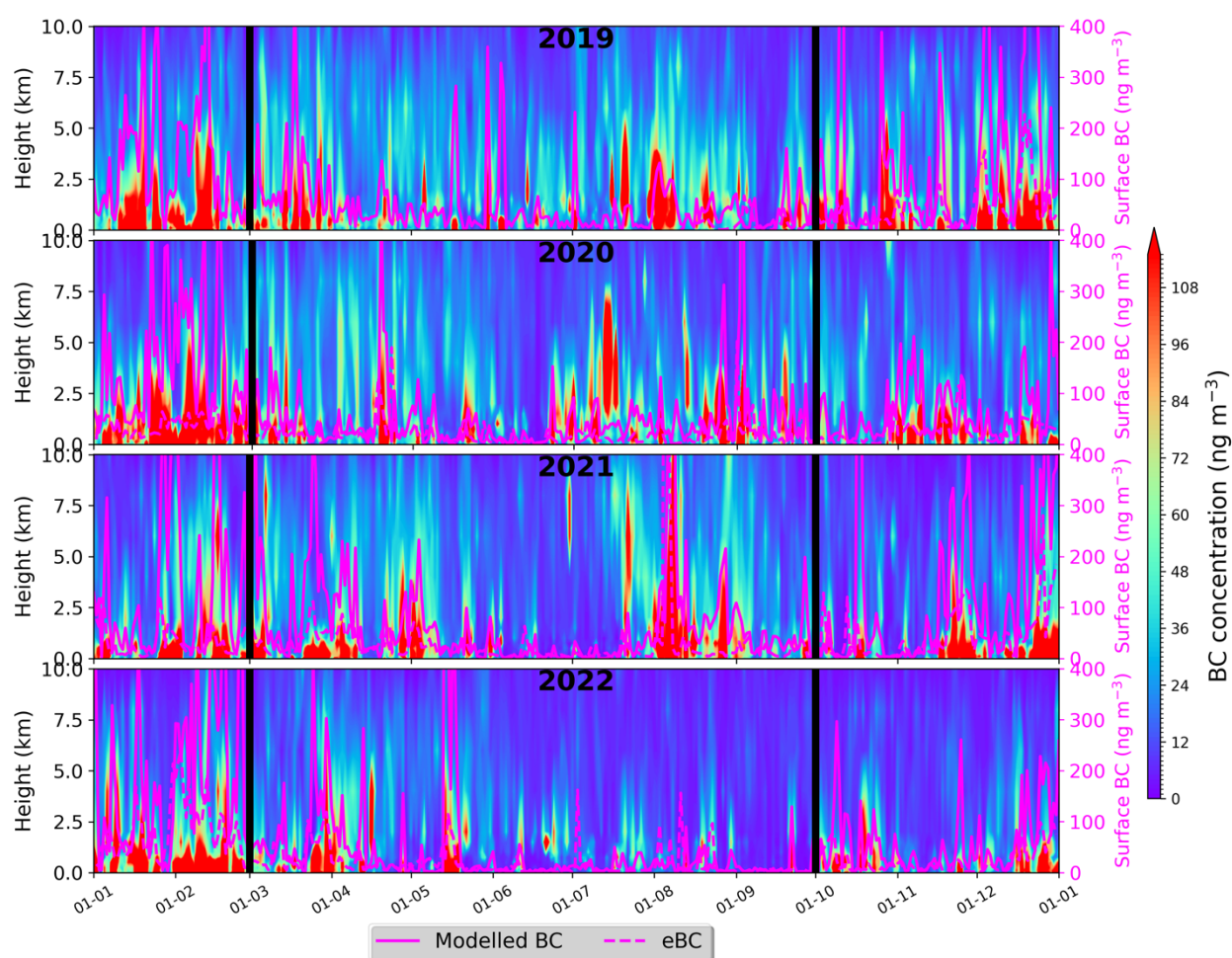


Figure 8. Vertical cross-sections of modelled BC for 2019-2022. Solid and dotted gray lines represent modelled daily surface BC and *eBC*, respectively. Their levels correspond to the right (secondary) axis (also in gray). Boundaries between the cold (November- April) and warm (May- October) are indicated by thick vertical black lines.

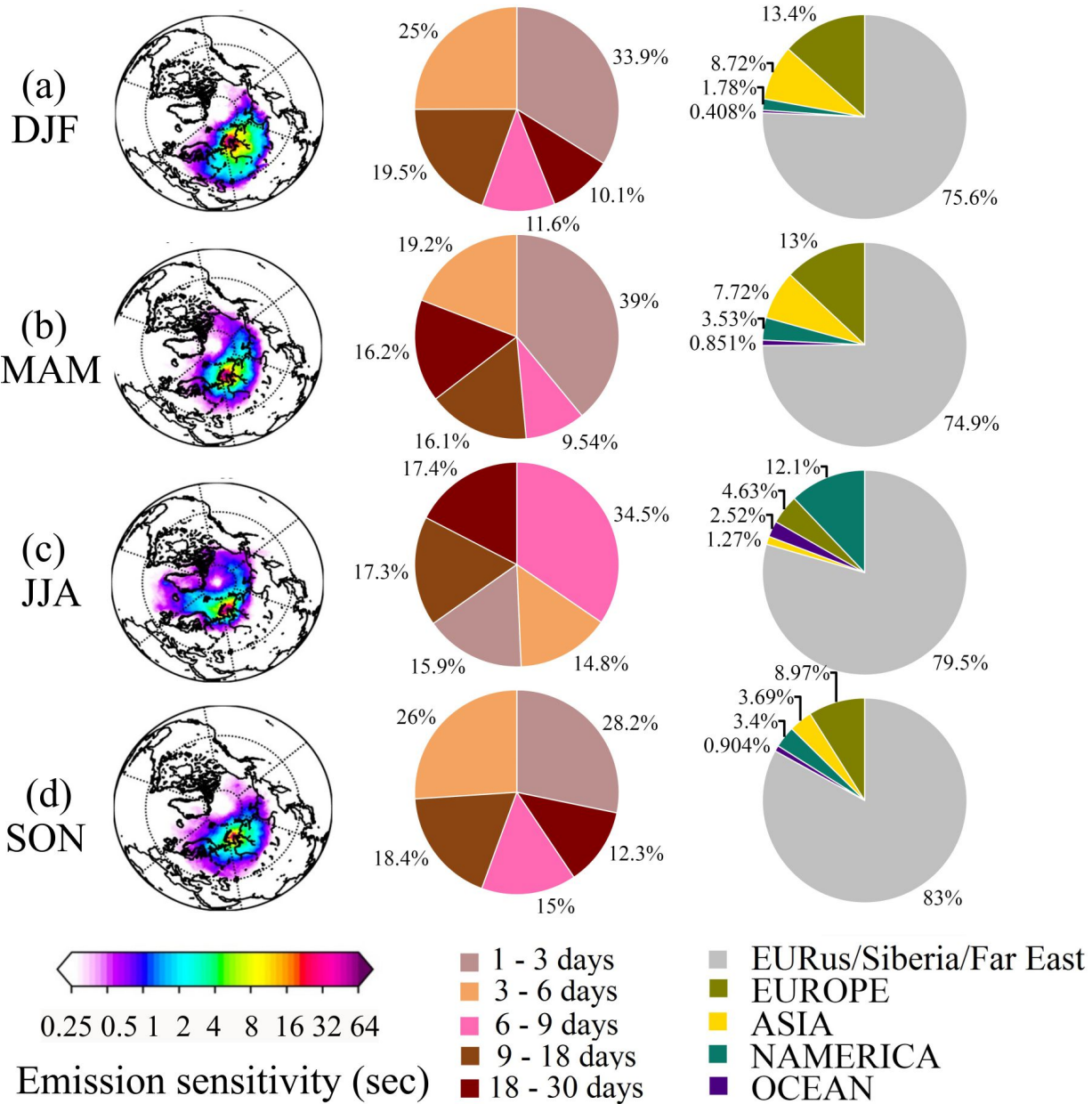


Figure 9. (a-d) Season average footprint emission sensitivity, mean age contribution of emissions from different day-periods back in time and each region contribution to surface concentration of BC.

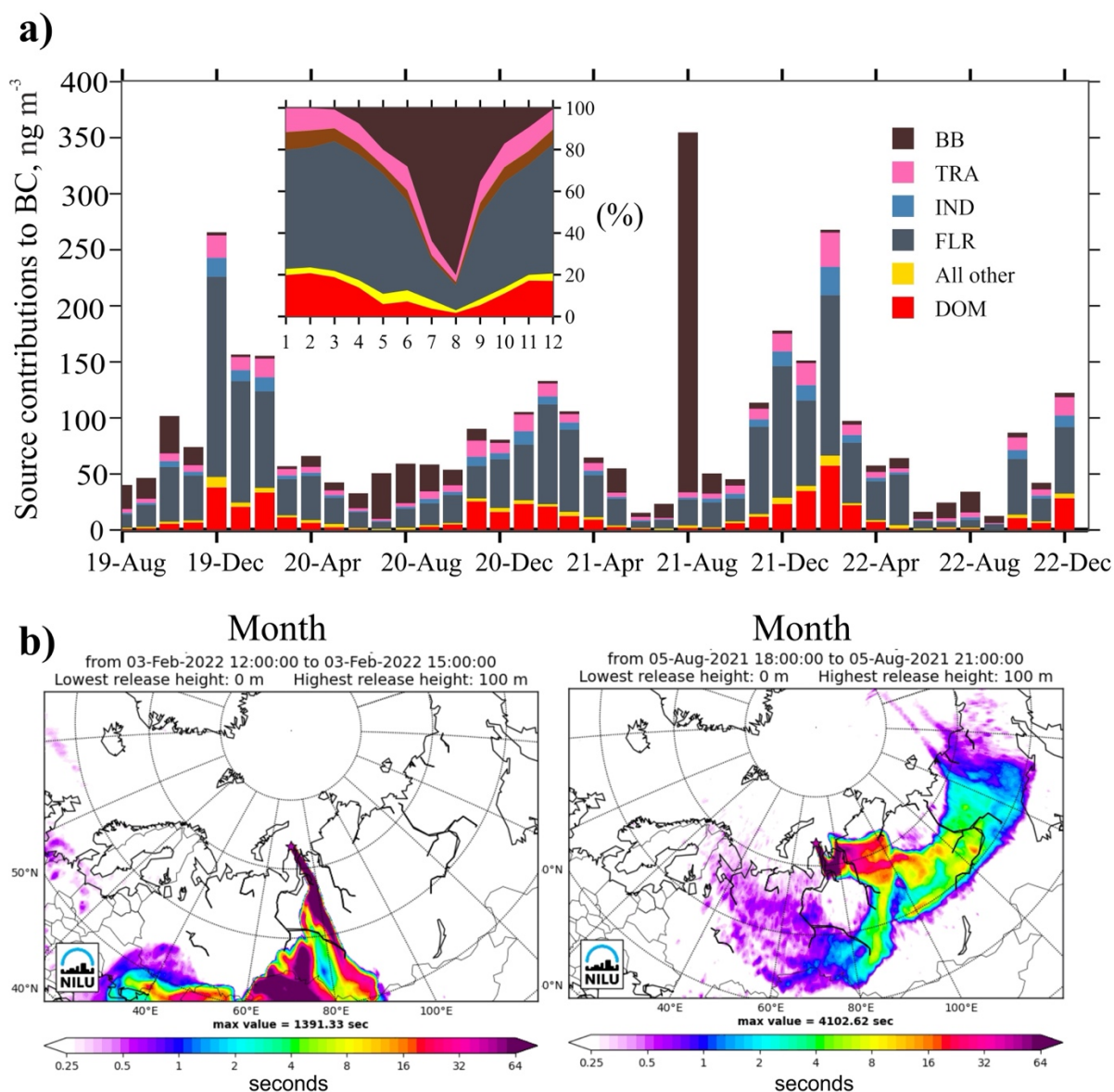


Figure 10. (a) Timeseries of monthly mean contribution from different emission source types to surface BC concentrations for the study period. DOM, BB, TRA, IND, FLR sectors, and All others sources were adopted from ECLIPSEv6 and CAMS GFAS. (b) FES for 3 February 2022 and 5 August 2021 showing the largest probability of emission origin.

TABLES & LEGENDS

Table 1. Statistics of light - absorption coefficients; EC, OC, eBC_{AET} , and eBC mass concentration; absorption Angstrom exponents (AAE) for the study period, cold and warm periods. Mean \pm standard deviation (1σ), 1st and 3rd Q quartile (25th and 75th percentiles).

Variable	August 2019 - December 2022				cold (November-April)				warm (May-October)			
	mean \pm sd	median	1 st Q	3 rd Q	mean \pm sd	median	1 st Q	3 rd Q	mean \pm sd	median	1 st Q	3 rd Q
$b_{abs}(880)$ (Mm ⁻¹)	0.5 \pm 0.9	0.3	0.1	0.6	0.7 \pm 0.7	0.5	0.22	0.9	0.4 \pm 0.9	0.2	0.09	0,4
$b_{abs}(520)$ (Mm ⁻¹)	0.9 \pm 1.6	0.4	0.2	1	1.2 \pm 1.2	0.8	0.38	1.5	0.6 \pm 1.8	0.3	0.1	0,6
$b_{abs}(370)$ (Mm ⁻¹)	1.2 \pm 2.4	0.6	0.3	1.4	1.6 \pm 1.6	1.1	0.52	2.1	0.9 \pm 2.8	0.4	0.2	0,9
EC (ng m ⁻³)	30 \pm 30	20	10	50	50 \pm 30	40	20	60	20 \pm 30	20	10	30
OC (ng C m ⁻³)	459 \pm 300	400	300	500	400 \pm 200	400	300	500	500 \pm 400	400	300	600
* eBC_{AET} (ng m ⁻³)	65 \pm 83	36	16	80	84 \pm 90	57	25	115	53 \pm 158	23	10	45
* eBC (ng m ⁻³)	29 \pm 54	13	5	34	44 \pm 47	29	12	59	19 \pm 57	8.0	4	17
$AAE_{370/950}$	0.96 \pm 0.6	0.95	0.7	1.19	0.94 \pm 0.4	0.95	0.74	1.1	0.98 \pm 0.8	0.95	0.6	1,3
$AAE_{370/520}$	1.0 \pm 1.5	0.93	0.4	1.52	0.88 \pm 1	0.89	0.49	1.2	1.16 \pm 1.9	1.0	0.3	2,0

* eBC_{AET} is defined in section 2.2.

** eBC is defined in section 3.2.